RSC Advances

PAPER

View Article Online
View Journal | View Issue

Cite this: *RSC Adv.*, 2025, **15**, 31471

Multifunctional PVDF membranes incorporating graphene, TiO_2, and nanocellulose: synergistic effects on filtration and antifouling performance

Anthonette James,[a] Md Rezaur Rahman,*[a] Khairul Anwar bin Mohamad Said,[a] Murtala Namakka,[a] M. Shahabuddin,[b] Muneera S. M. Al-Saleem,[c] Jehan Y. Al-Humaidi,[c] Mohammed M. Rahman[d] and Mohammed Abdus Salam[e]

Methylene blue (MB) remains one of the most resilient contaminants in industrial wastewater which presents serious threats to both environmental integrity and human health. Its high chemical stability and resistance to natural degradation render most conventional treatment methods ineffective. As such, this study aimed to develop a multifunctional nanocomposite membrane that mitigates membrane fouling, enhances dye separation, and improves water permeability. Correspondingly, a modified phase inversion method was employed to fabricate polyvinylidene fluoride (PVDF) membranes reinforced with bamboo-derived nanocellulose (NC), titanium dioxide (TiO_2), and varying graphene (GR) contents (0–1 wt%). Characterization through FTIR confirmed the successful integration of GR through the attenuation of semi-ionic C–F bonds and the emergence of C═C stretching bands while XRD results revealed that all membranes retained their β-phase crystallinity with slight enhancements in peak intensity attributed to structural modification by GR. Besides, FESEM and EDX analyses revealed that GR-loaded membranes exhibited improved pore morphology, greater surface porosity, and increased carbon content, with average pore size rising from 4.89×10^{-3} µm to 13.56×10^{-3} µm and porosity from 79.68% to 84.86%, indicating enhanced structural openness, interconnectivity, and effective GR dispersion within the membrane matrix. Experimental results revealed that the membrane with 0.6 wt% GR (PVDF-NC/TiO_2/GR3) achieved a balanced performance with superior pore interconnectivity contributing to water permeation flux of 270.74 L m^{-2} h^{-1}. This pore architecture favoured water transport without significant loss in selectivity. In terms of separation performance, the 0.4 wt% GR membrane achieved the highest dye rejection of 97% and a flux recovery ratio (FRR) of 98%, which confirmed its strong antifouling properties under UV irradiation. The adsorption behaviour was best described by the Langmuir isotherm model with high correlation coefficients (R^2 = 0.85 to 0.99), indicating monolayer dye uptake on uniform active sites. The PVDF-NC/TiO_2/GR3 showed the highest adsorption capacity (Q_{max} = 1.866 mg g^{-1}), supported by R^2 = 0.96. In contrast, the control membrane (PVDF-NC/TiO_2) exhibited the strongest dye-binding affinity (K_L = 478 L mg^{-1}, R^2 = 0.97). Overall, this study introduces a practical nanocomposite membrane that effectively mitigates the conventional trade-off between permeability and selectivity by delivering high dye removal, strong antifouling performance, and promising applicability for industrial wastewater treatment. Comparative analysis with previously reported PVDF-based membranes further highlighted the superior performance of the developed formulation.

Received 1st July 2025
Accepted 12th August 2025

DOI: 10.1039/d5ra04672f

rsc.li/rsc-advances

1 Introduction

The pervasive contamination of water sources by synthetic dyes represents a critical environmental challenge with far reaching ecological and public health implications. According to Al-Tohamy *et al.*,[1] the presence of synthetic dyes in industrial wastewater continues to pose a serious threat to public health and aquatic ecosystems owing to their toxic, mutagenic, and carcinogenic properties. These pollutants exhibit exceptional persistence in aqueous environments by resisting natural degradation processes and accumulating in the food chain.[2]

---

[a] *Department of Chemical Engineering and Energy Sustainability, Universiti Malaysia Sarawak, Malaysia. E-mail: rmrezaur@unimas.my*

[b] *Department of Mechanical Engineering, Faculty of Engineering, University of Malaya, 50603 Kuala Lumpur, Malaysia*

[c] *Department of Chemistry, Science College, Princess Nourah Bint Abdulrahman University, P. O. Box 84428, Riyadh 11671, Saudi Arabia*

[d] *Center of Excellence for Advanced Materials Research (CEAMR), Chemistry Department, Faculty of Science, King Abdulaziz University, Jeddah 21589, Saudi Arabia*

[e] *Department of Environmental Science and Disaster Management, Noakhali Science and Technology University, Bangladesh*

The discharge of MB dye, one of the most persistent dyes from textile, pharmaceutical, and paper industries, is particularly problematic owing to the global production of this dye exceeds 10 000 tons annually.[3] Its molecular structure confers high solubility, chemical stability, and resistance to biodegradation which eventually creating significant challenges for conventional water treatment systems.[4] Additionally, the toxicological profile of MB includes acute effects such as skin irritation, respiratory distress, and disruption of aquatic photosynthesis along with chronic impacts on metabolic and reproductive functions in aquatic organisms.[5] The significant escalation in dye contamination which driven by increasing global industrial activities have created an urgent need to advanced remediation techniques.[6]

According to Abdul Rahman *et al.*,[7] current water treatment infrastructure relies heavily on conventional processes including coagulation, biological oxidation, and activated carbon adsorption for contaminant removal. Although these methods demonstrate efficacy for certain pollutants, such undertaken exhibit fundamental limitations in addressing persistent micro contaminants, particularly at low concentration between 1 to 100 ppm commonly found in industrial effluents.[8] As reported in study conducted by Fito *et al.*,[3] the molecular stability and cationic nature of methylene blue could render its resistant to biological degradation while its solubility limits adsorption efficiency. Furthermore, these conventional systems face operational challenges including high chemical consumption, frequent regeneration requirements, significant sludge generation, and susceptibility to fouling which substantially increasing lifecycle costs.[6,7,9,10]

Membrane technology has emerged as a promising alternative for advanced water treatment owing to its controllable pore structure, selective separation capability, and potential for continuous operation.[11] As informed by ref. 12, pressure driven membrane processes, particularly reverse osmosis, nanofiltration, and ultrafiltration have demonstrated superior dye rejection capabilities with over 90% in comparison to conventional methods. However, polymeric membranes often face intrinsic limitations, most notably the permeability selectively-relationship, where high dye rejection typical reduces water flux and subsequently leading to compromised treatment efficiency.[8] Besides, membrane fouling remains a persistent challenge due to the foulant accumulation reduces permeate flow, increases maintenance requirements as well as necessitates chemical cleaning that damages the membrane structure.[13] These limitations are exacerbated in real wastewater sources containing complex mixtures of contaminants, salts, and organic matter.[14,15]

In order to mitigate these limitations, nanotechnology enhanced membranes represent a paradigm shift in water treatment systems. Recent developments suggest that the application of nanomaterials with hydrophilic, antibacterial, or photocatalytic properties into membrane structures could significantly reduce fouling while improving the contaminant separation process.[16] These nanocomposite membranes offer a promising route to overcome the permeability-selectivity trade off while supporting antifouling functions in order to make such membrane attractive for industrial applications.[17] A multifunctional membrane could leverage the synergistic interactions between several components in which nanocellulose provides mechanical reinforcement and water transport channels, TiO_2 offers photocatalytic degradation capabilities, and pristine graphene enhances adsorption capacity and electrical conductivity.[18–20] Several studies in the published literature have incorporated functional nanomaterials into polymer matrices in order to enhance structural integrity and filtration performance.[12,21,22] As reported by Akram *et al.*,[20] carbon-based materials have demonstrated exceptional promise owing to its tuneable surface chemistry and unique two-dimensional structure. Bamboo-derived nanocellulose presents a sustainable and biodegradable reinforcement material with high tensile strength of 7.6 GPa and surface area up to 500 $m^2\ g^{-1}$.[18] The sustaining sourcing of this natural material from abundant lignocellulosic biomass aligns with green chemistry principles and reduces environmental impact compared to synthetic nanomaterials.[5]

Although these nanomaterials have been individually explored in membrane design, its combined application within a single polymer matrix remains under investigated.[12] Most prior works focus on binary filler systems, namely nanocellulose-TiO_2 or graphene TiO_2, or lacks optimization of interfacial interactions.[22] Limited studies have validated the functional synergy of NC, TiO_2, and GR within with PVDF membranes under real dye exposure conditions, particularly regarding long-term stability and fouling resistance.[15] As such, this study proposes a multifunctional membrane composed of PVDF reinforced with bamboo-derived NC, TiO_2, and GR. Such hybrid membrane is fabricated by using a modified phase inversion process which designed to enhance filler dispersion, pore uniformity, and membrane durability. Correspondingly, the objectives of this study are to (i) fabricate nanocomposite membranes with integrated fillers and characterize their structural morphological, and compositional features, (ii) investigate the effect of graphene content on pore development, surface roughness, and elemental uniformity, (iii) evaluate the membrane water permeability, dye rejection efficiency, and antifouling performance under methylene blue exposure, and (iv) analyze the adsorption behaviour using established isotherm models to determine the dominant removal mechanism. By integrating multiple functionalities into a single membrane structure, this study advances nanocomposite membrane technology toward industrial implementation while addressing environmental sustainability through the utilization of bamboo nanocellulose and energy efficient photocatalytic processes.

2 Materials and methods

2.1 Materials and chemicals

Bamboo NC used in this study was extracted from *Gigantochloa scortechinii* as reported in the previous work (A. James *et al.*, 2024). It was chosen due to its abundance in Borneo, low toxicity, biocompatibility, high aspect ratio and tunable surface chemistry, all of which contribute beneficial physical properties to the membrane development.[15] The outstanding chemical resistance, mechanical robustness and thermal stability of poly(vinylidene fluoride) (PVDF) (CAS No: 24937-79-9, molecular weight: 534 000 g mol^{-1}) supported its selection as the primary polymer matrix for fabricating high-performance membranes in this study.[23] PVDF was obtained from Sigma-Aldrich Sdn. Bhd. (Petaling Jaya, Malaysia). Additional chemicals such as titanium(IV) oxide (TiO_2) (CAS No: 13463-67-7), dimethylacetamide (DMAc) (CAS No: 127-19-5), lithium chloride (LiCl) (CAS No: 7447-41-8) and graphene powder (1034343-98-0) were also sourced from Sigma-Aldrich Sdn. Bhd. (Petaling Jaya, Malaysia). TiO_2 was employed as a photocatalytic additive, offering self-cleaning properties under UV light exposure by generating reactive oxygen species capable of degrading organic foulants on the membrane surface.[24,25] DMAc, a dipolar aprotic solvent, was selected for its effectiveness in dissolving PVDF and ensuring uniform homogeneous nanoparticles dispersion in the casting dope solution during membrane preparation.[26,27] LiCl was utilized to influence the phase separation process by adjusting the thermodynamic and kinetic behaviour of the casting solution. Its inclusion enhanced efficient solvent–nonsolvent exchange, improved membrane hydrophilicity, and promoted the formation of a highly porous and interconnected structure, thereby enhancing water flux and fouling resistance (A. James *et al.*, 2024). Ultrapure and deionized (DI) water used throughout the experimental procedures were supplied by Universiti Malaysia Sarawak (UNIMAS). All chemicals used were of analytical grade.

2.2 Fabrication of nanocomposite membrane *via* phase inversion technique

The nanocomposite membranes were fabricated using the phase inversion technique with modifications based on previously established procedures.[28,29] To initiate the membrane fabrication process, the desired amount of GR as specified was accurately measured and dispersed in half of the total weight of DMAc solvent in a conical flask, following procedures reported in the literature.[30] This mixture was referred to as the GR solution. The conical flask was then placed in a particle homogenizer with a water bath and agitated at 80 °C and 250 rpm for 1 hour in order to ensure a uniform and stable dispersion of GR. Concurrently, the remaining portion of the DMAc was used to dissolve LiCl at 70 °C and 100 rpm. After the LiCl was completely dissolved, NC was gradually added until a homogeneous solution was formed according to the method described in the previous work.[31] This step was intended to ensure a uniform distribution of NC, enhance membrane porosity and reduce the tendency for NC agglomeration. The resulting solution was labelled as the NC solution.

Following these steps, the GR solution was combined with the NC solution and thoroughly mixed to achieve a uniform mixed solution. TiO_2 nanoparticles were subsequently added at a fixed loading of 3 wt% relative to the PVDF weight. This concentration was selected based on prior findings, which identified 3 wt% as the optimum level for improving antifouling and photocatalytic performance in the resulting PVDF-NC/TiO_2 nanocomposite membranes. PVDF pellets were gradually added to the mixed solution to form the PVDF-NC/TiO_2/GR dope solution. The resulting dope solution was continuously stirred at a constant temperature of 50 °C and 350 rpm for 24 hours to ensure complete dissolution of PVDF, promote uniform mixing of all components, and eliminate trapped air. The specific compositions of the control and GR-incorporated nanocomposite membrane formulations were prepared based on the weight ratios listed in Table 1.

Once the 24-hour dope solution mixing process was completed, approximately 10 ml of the solution was carefully poured onto a glass plate with a measurement of 21 cm × 30 cm and cast at room condition. The cast film was immediately immersed in a first coagulation bath containing DI water for 20 minutes to initiate phase separation and promote the solidification of the nanocomposite membrane through solvent and non-solvent exchange process. The partially solidified membrane was then transferred to a second DI water bath and left undisturbed for an additional 24 hours to remove excess solvent retained within the membrane matrix which could have potentially affected membrane integrity and performance. Finally, the membranes were placed in a clean container, immerse in ultrapure water and stored in a refrigerator at 5 °C until further characterization and performance evaluation were conducted.

2.3 Morphological, structural and chemical characterization of nanocomposite membranes

2.3.1 Fourier transform infrared spectroscopy (FTIR) analysis. A Fourier-transform infrared (FTIR) spectrometer (IRAffinity-1, Shimadzu, Japan) was employed to analyse the molecular bond structures and functional groups present in the membrane samples. Measurements were conducted using the attenuated total reflectance (ATR) mode, covering a spectral range from 4000 to 400 cm^{-1} with a resolution of 4 cm^{-1} and 32 scans per sample. A solid membrane sample measuring approximately 1 cm × 1 cm was cut and positioned on the ATR crystal platform. The sample was then secured using a swivel press to ensure firm contact between the membrane surface and the crystal. Both qualitative and quantitative interpretations of the obtained spectra were conducted in accordance with ASTM E1252-98 (2021) and ASTM E168-16 (2016) standards.[32,33]

2.3.2 X-ray diffraction (XRD) analysis. X-ray diffraction (XRD) analysis was conducted to investigate the crystallinity and phase composition of the nanocomposite membrane samples. The analysis was performed at room temperature using a Rigaku SmartLab Powder X-ray diffractometer equipped with CuKα radiation (λ = 1.5418 Å). The diffraction patterns were recorded across a 2θ range of 5° to 80° at a scanning rate of 2° min^{-1}. The degree of crystallinity was assessed by calculating the crystalline index (Crl) using the following empirical relationship in eqn (1):

$$\text{Crystalline index}(\%) = \frac{\text{Area of all the crystalline peak}}{\text{Area of all crystalline + amorphous peaks}} \times 100 \quad (1)$$

Table 1 Dope solution formulations

Nanocomposite membranes	PVDF (wt%)	NC (wt%)	TiO_2 (wt%)	GR (wt%)	LiCl (wt%)	DMAc (wt%)
PVDF-NC/TIO_2	15	0.6	0.45	0	0.34	83.61
PVDF-NC/TIO_2/GR1	15	0.6	0.45	0.2	0.34	83.58
PVDF-NC/TIO_2/GR2	15	0.6	0.45	0.4	0.34	83.55
PVDF-NC/TIO_2/GR3	15	0.6	0.45	0.6	0.34	83.52
PVDF-NC/TIO_2/GR4	15	0.6	0.45	0.8	0.34	83.49
PVDF-NC/TIO_2/GR5	15	0.6	0.45	1.0	0.34	83.46

Additionally, the crystallite size (D) was estimated using the Debye–Scherrer equation as derived in eqn (2).

$$D = \frac{k\lambda}{\beta \cos \theta} \tag{2}$$

where k is the Scherrer constant (0.94); λ is the X-ray wavelength (1.5418 nm); β is the full width at half maximum (FWHM) in radians and θ is the Bragg angle.

All procedures were carried out in accordance with the ASTM F3419-22 (2022) standard.[34]

2.3.3 Field emission scanning microscopy (FESEM) and energy dispersive X-ray (EDX) analysis. The surface and cross-sectional morphologies of the nanocomposite membrane samples was examined using a Hitachi S-4700 Field Emission Scanning Electron Microscope (FESEM) integrated with an energy-dispersive X-ray (EDX) spectroscopy. Prior to imaging, the membrane samples were precisely cut into uniform rectangular pieces for surface and cross-sectional analysis. The cross-sectional specimen was prepared by immersing the membrane sheet in liquid nitrogen, followed by cryogenic fracturing to preserve internal morphology and minimize mechanical distortion. Both surface and cross-sectional specimens were sputter-coated with a thin, uniform layer of gold (Au) using a JFC-1600 coater (JEOL, Japan) which operated at 15 mA for 60 seconds in a single coating cycle. This process produced an estimated coating thickness of approximately 10 nm to ensure optimal surface conductivity and imaging resolution during FESEM analysis. Each specimen was then mounted onto aluminium stubs using conductive adhesive for examination. Morphological images were obtained using a field emission gun operated at an accelerating voltage of 20 kV. The procedure was carried out in accordance with the guidelines outlined in ASTM E3-11 (2017).[35] While FESEM was utilized to investigate the structural features of the membrane surface, energy-dispersive X-ray spectroscopy (EDX) was employed to determine the elemental composition in the samples.

2.3.4 Determination of nanocomposite membrane porosity and mean pore size. The porosity (ε) of the nanocomposite membrane was measured *via* the gravimetric method as stated in a previously reported study and calculated based on the following eqn (3).[36]

$$\varepsilon\% = \frac{\left(\dfrac{W_{\text{wm}} - W_{\text{dm}}}{\rho_{\text{water}}}\right)}{\left(\dfrac{W_{\text{wm}} - W_{\text{dm}}}{\rho_{\text{water}}}\right) + \left(\dfrac{W_{\text{dm}}}{\rho_{\text{PVDF}}}\right)} \times 100 \tag{3}$$

where w_{wm} is the weight of wet membrane (g); w_{dm} is weight of dry membrane (g); ρ_{water} is the density of water (0.998 g cm^{-3}) and ρ_{PVDF} is the density of PVDF polymer (1.740 g cm^{-3}).

The average pore size of the nanocomposite membrane was estimated using the Guerout–Elford–Ferry equation as stated in the literature.[37] The mean pore radius was derived from eqn (4), while the mean pore diameter was calculated by doubling the radius value as shown in eqn (5).

$$\text{Mean pore radius} = \sqrt{\frac{(2.9 - 1.75\varepsilon) \times 8\eta l Q}{\varepsilon \times A \times \Delta P}} \tag{4}$$

where ε is the membrane porosity (%); η is the water viscosity (0.00089 Pa.s); l is the membrane thickness (m); Q is the volume of water permeation (m^3 s^{-1}); A is the effective area of membrane (m^2) and ΔP is the pressure applied (Pa).

$$\text{Mean pore size (nm)} = 2 \times \text{mean pore radius} \tag{5}$$

2.3.5 Ultraviolet-visible (UV-vis) spectroscopy analysis. UV-vis analysis was performed on all collected permeate samples to determine the final concentration of MB dye following the filtration process using the respective nanocomposite membranes. A volume of approximately 5 ml from each permeate sample was transferred into a UV-vis cuvette and inserted into the UV-visible spectrophotometer for analysis. The absorbance measurement for the MB dye solution was conducted within the wavelength range of 500 to 700 nm. A calibration curve was generated using standard solutions with known concentrations of MB (0.1, 0.2, 0.5, and 1.0 ppm). This procedure was carried out in compliance with ASTM E169-16 (2022).[38]

2.4 Effect of graphene incorporation on the performance of PVDF/NC/TiO_2 nanocomposite membranes

The analyses were conducted in three sequential stages to evaluate the performance of the developed nanocomposite membrane in terms of water permeability, MB dye selectivity and photocatalytic activity with detailed experimental conditions provided in the respective subsections.

2.4.1 Water permeation flux performance of nanocomposite membranes. Following the previous work, each nanocomposite membrane was cut into a 4.4 cm diameter disc, sufficient to cover the effective membrane filtration area of 1.52 × 10^{-3} m^2. The cut membrane was then mounted onto the membrane holder of the water filtration equipment as described in the earlier study.[29] The membrane was held firmly in place using a rubber O-ring which was secured by fastening the membrane holder cover. Approximately 2 L of water was poured into the solution tank of the water filtration equipment. Prior to conducting the actual measurements, the membrane underwent pre-compression at 2 bar for 30 minutes to stabilise the initial water flux. Following this, the operating pressure was reduced to 1 bar, and the volume of permeate was recorded at 10-minute intervals over a 70-minute period. The collected water permeation flux was calculated based on the ratio of permeate volume to the corresponding permeation time by using eqn (6).[37] To enhance accuracy, each membrane sample was tested five times and the average permeation flux values were calculated for each time interval.

$$J_{\mathrm{W}} = \frac{V}{A \times \Delta T} \tag{6}$$

where J_{W} is the pure water permeation flux (L m^{-2} h^{-1}); V is the permeate volume (m^3); A is the effective area of membrane (m^2) and ΔT is the filtration time (h).

2.4.2 MB dye selectivity of nanocomposite membranes. Initially, the 1 ppm concentration of MB dye was prepared and verified using a UV-160 UV-vis-NIR spectrophotometer (Shimadzu Scientific Instruments, Inc., Tokyo, Japan). Following the previous procedure, the water sample in the solution tank was replaced with the prepared MB dye solution as the feed solution for the membrane rejection analysis. The tested membrane was operated at 1 bar pressure under room conditions. The permeate (J_{MB}) was collected at 10-minute intervals over a 70-minute timeframe and the corresponding volumes were recorded. The MB dye removal ratio (R) was calculated by employing eqn (7) as described in a study.[39] To ensure data reliability and reproducibility, each membrane sample was subjected to five independent dye removal tests and the average removal efficiency was reported.

$$\%R = \left(1 - \frac{C_{\mathrm{f}}}{C_{\mathrm{i}}}\right) \times 100 \tag{7}$$

where R is the dye removal ratio (%); C_{f} is the final MB dye concentration (mg L^{-1}) and C_{i} is the initial MB dye concentration (mg L^{-1}).

2.4.3 Photocatalytic activity and antifouling performances of nanocomposite membranes. After the sequential dye rejection procedure, each nanocomposite membrane underwent photocatalytic testing under visible UV-light irradiation to assess its self-cleaning performance as describe in the previous work.[29] The previously used membrane was placed in a Petri dish containing 50 ml of DI water and exposed to a 100 W UV lamp positioned 5 cm above the membrane surface for 24 hours in a dark environment. Following the UV treatment, the membrane was subjected to a second water permeation flux test (J_{W2}) under the same operating conditions as before. The flux recovery ratio (FRR) was calculated using eqn (8).[39]

$$\mathrm{FRR} = \left(\frac{J_{\mathrm{w2}}}{J_{\mathrm{w}}}\right) \times 100\% \tag{8}$$

where J_{W} is the initial pure water permeation flux (L m^{2-} h^{-1}) and $\mathrm{J_{W2}}$ is the pure water permeation flux after photocatalytic activity.

2.5 Formulation of adsorption isotherm for MB dye uptake by nanocomposite membranes

An initial MB dye concentration of 1 ppm was used in all adsorption experiments and the residual concentrations in the permeate were determined by utilizing UV-vis spectroscopy analysis. The obtained data were used to formulate two adsorption isotherm models, particularly the Langmuir and the Freundlich, based on the assumption of each model regarding adsorption mechanisms and surface characteristics of the nanocomposite membranes.

2.5.1 Langmuir isotherm. The Langmuir adsorption isotherm was employed to evaluate the adsorption characteristics of MB dye molecules onto the developed PVDF-NC/TiO_2 and PVDF-NC/TiO_2/GR nanocomposite membranes under equilibrium conditions at 25 °C. Based on the literature, this model assumed monolayer adsorption onto a homogeneous surface possessing a finite number of energetically uniform and identical active sites. The non-linear form of the Langmuir equation was expressed by eqn (9).[40]

$$q_{\mathrm{e}} = \frac{Q_{\max} K_{\mathrm{L}} C_{\mathrm{e}}}{1 + K_{\mathrm{L}} C_{\mathrm{e}}} \tag{9}$$

where q_{e} is the quantity of dye adsorbed per unit mass of nanocomposite membrane at equilibrium (mg g^{-1}); C_{e} is the concentration of MB dye at equilibrium (mg L^{-1}); $Q_{\max}$ is the maximum monolayer adsorption capacity of the nanocomposite membrane (mg g^{-1}); K_{L} is the Langmuir constant that reflects the affinity between MB molecules and the active sites (L mg^{-1}).

To facilitate parameter estimation *via* linear regression, the Langmuir isotherm was linearized as displayed in eqn (10).[10]

$$\frac{C_{\mathrm{e}}}{q_{\mathrm{e}}} = \frac{1}{Q_{\max}} C_{\mathrm{e}} + \frac{1}{K_{\mathrm{L}} Q_{\max}} \tag{10}$$

This linearised equation allowed for the estimation of $Q_{\max}$ and K_{L} based on the slope and intercept generated from the linear plot of $\frac{C_{\mathrm{e}}}{q_{\mathrm{e}}}$ against C_{e}. The obtained correlation coefficient (R^2) was used to evaluate the goodness of fit of the Langmuir model.

2.5.2 Freundlich isotherm. The Freundlich isotherm model was further employed to determine the adsorption behaviour of MB dye molecules onto the developed PVDF-NC/TiO_2 and PVDF-NC/TiO_2/GR nanocomposite membranes by taking into account the heterogeneous nature of the membrane surface which allowed for a non-uniform distribution of adsorption energies and potential formation of multilayer adsorption. The non-linear form of the Freundlich equation was expressed by eqn (11).[41]

$$q_{\mathrm{e}} = K_{\mathrm{f}} C_{\mathrm{e}}^{\frac{1}{n}} \tag{11}$$

where q_e is the quantity of dye adsorbed per unit mass of nanocomposite membrane at equilibrium (mg g^{-1}); K_f is the Freundlich constant indicating multilayer adsorption capacity (L mg^{-1}); C_e is the concentration of MB dye at equilibrium (mg L^{-1}) and $\frac{1}{n}$ is the Freundlich adsorption intensity.

To facilitate parameter estimation *via* linear regression, the Freundlich isotherm was linearized as displayed in eqn (12).[42]

$$\log q_e = \log K_f + \frac{1}{n}\log C_e \tag{12}$$

This linearised equation allowed for the estimation of $\frac{1}{n}$ and $\log K_f$ based on the slope and intercept generated from the linear plot of $\log q_e$ against $\log C_e$. The obtained correlation coefficient (R^2) was used to evaluate the goodness of fit of the Freundlich model.

2.5.3 Statistical analysis. The accuracy of each isotherm model was evaluated using a statistical parameter, R^2, which reflected the degree of agreement between the experimental data and the model predictions. The mathematical expression for R^2 was provided in eqn (13).[43]

$$R^2 = 1 - \frac{\sum_{i=1}^{n}\left(q_{e,\exp} - q_{e,\text{model}}\right)^2}{\sum_{i=1}^{n}\left(q_{e,\exp} - \overline{q}_{e,\exp}\right)^2} \tag{13}$$

where $q_{e,\exp}$ is the experimental adsorption capacity at equilibrium (mg g^{-1}); $q_{e,\text{model}}$ is the predicted adsorption capacity at equilibrium based on the isotherm model; $\bar{q}_{e,\exp}$ is the mean of all experimentally observed values and n is the total number of data points.

The R^2 was expected to range between 0 to 1, with higher values indicating a stronger correlation between the experimental data and the model predictions. In this study, R^2 value exceeding 0.75 was regarded as the benchmark for a satisfactory model fit. This criterion was widely accepted in adsorption studies, as it suggested that the model accounted for more than 75% of the variability in the experimental results, reflecting a high level of predictive accuracy.[9,10,44]

3 Results and discussion

3.1 FTIR analysis of functional groups in PVDF-NC/TiO$_2$ and GR-incorporated nanocomposite membranes

The FTIR analysis shown in Fig. 1 was conducted to identify the main functional groups present in all nanocomposite membranes and observe the influence of incorporating GR towards the functional groups of the PVDF-NC/TiO$_2$/GR membranes. The analysis revealed that the inclusion of GR into the nanocomposite membrane significantly attenuated the peak intensities within the spectral region of 1500–800 cm^{-1}. This range corresponded to the presence of C–F bonds in the PVDF matrix which were associated with semi-ionic bonding.[29,45] As reported in the literature, the regular arrangement of –CF$_2$ groups along the PVDF backbone contributes to its semi-crystalline nature.[46] In the present study, the intensity of the characteristic C–F stretching vibration of PVDF decreased with increasing GR loadings in S1 to S5 in the PVDF-NC/TiO$_2$/GR nanocomposite membranes. This observation may be attributed to the introduction of more complex interfacial interactions arising from the presence of ternary nanofillers. In contrast, some studies have reported minimal changes in FTIR spectra upon the inclusion of a single nanofiller at low GR loadings into the PVDF matrix.[47,48] In the context of present work, the observed spectral changes suggested strong interfacial interactions between GR and PVDF chains, primarily initiated by the π–π stacking interactions between the aromatic rings of GR and the PVDF chains.[49] Previous studies have also shown that graphene interacted with polymer matrices through various non-covalent interactions, such as π–π stacking, hydrophobic associations, and electrostatic attractions, depending on the nature of the polymer and surface characteristics of the graphene.[50,51] Additionally, the presence of nanofillers such as NC and TiO$_2$ likely contributed to more intricate interfacial effects, further affecting the intensity of the C–F stretching bond. A slight broadening in the O–H stretching region around 3300–3400 cm^{-1} was detected which assigned to the hydroxyl groups naturally present in NC and the surface O–H groups on TiO$_2$ which originated from adsorbed water.[14,29] This feature suggested the potential for hydrogen bonding interactions between NC and the PVDF matrix or GR surface. A similar interaction may have occurred with TiO$_2$, particularly through its surface O–H groups which possibly facilitated the formation of hydrogen bridge bonds with the PVDF matrix. These interactions were primarily attributed to van der Waals forces between the TiO$_2$ nanoparticles and the PVDF chains, initiated by dipole–dipole and dipole-induced dipole interactions.[52] Such observation aligned with the previous reports discussing the interaction mechanism between TiO$_2$ and polysulfone-based composite membrane.[53]

In addition to the preceding discussion, the incorporation of GR into the PVDF nanocomposite membrane, the ordered semi-ionic C–F bonding network was altered through the interactions with the sp^2-hybridized carbon lattice of GR, promoting the formation of sp^3 C–F covalent bonds.[45,46] This transformation disrupted the local molecular order and contributed to changes in membrane crystallinity. This interpretation was further supported by the EDX results, where the content of F element decreased with the addition of GR, suggesting partial surface masking of the PVDF nanocomposite membranes by graphene nanoparticles. In conjunction, although the FTIR and EDX analyses suggested modifications in the local molecular order and partial surface masking, the XRD profile shown in Fig. 2 revealed no significant changes in peak position or intensity corresponding to the β-phase of the PVDF nanocomposite membranes. Based on the findings, the incorporation of GR did not significantly alter the bulk crystalline structure of the PVDF matrix, as confirmed by XRD patterns. The GR-incorporated nanocomposite membranes retained their semi-crystalline behaviour despite the surface-level modifications.

Additionally, a low intensity peak with moderate sharpness was detected at 1527 cm^{-1} alongside a broader band at 1697 cm^{-1}, both of which were assigned to C═C stretching

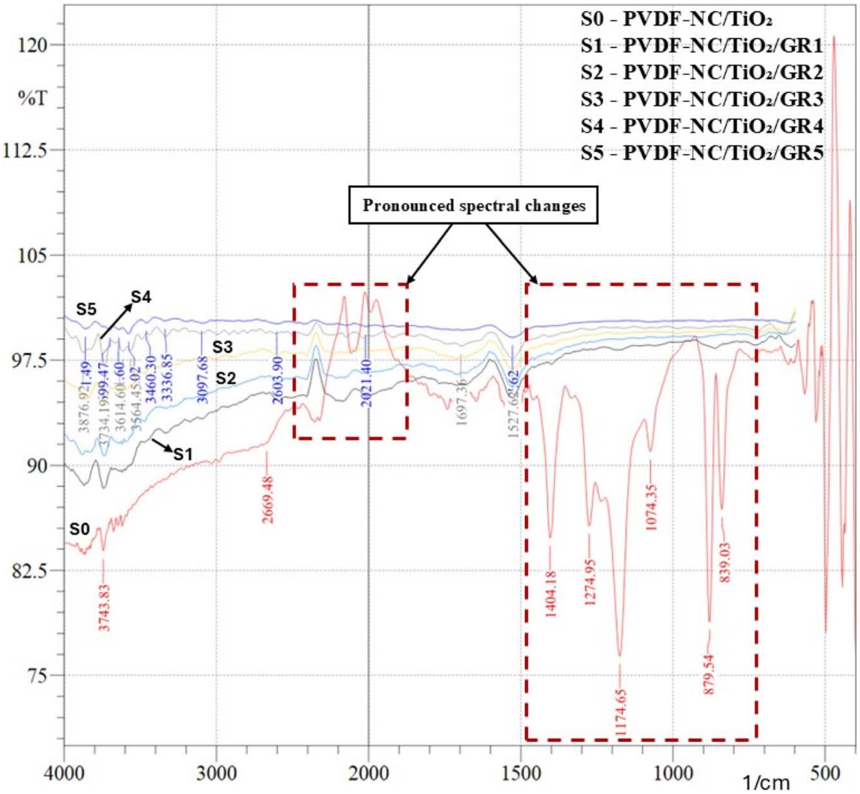

Fig. 1 FTIR spectra of the control nanocomposite membrane (PVDF-NC/TiO_2) and GR-incorporated nanocomposite membranes (PVDF-NC/TiO_2/GR) with varied GR loadings.

vibrations of aromatic ring associated with non-oxidized GR.[54,55] The intensity of the 1527 cm^{-1} peak became more pronounced with increasing GR loadings, reflecting the rising contribution of carbon nanostructures to the overall composition of the nanocomposite membrane.[56] Besides, the incorporation of GR also reduced the presence of oxygen-containing functional

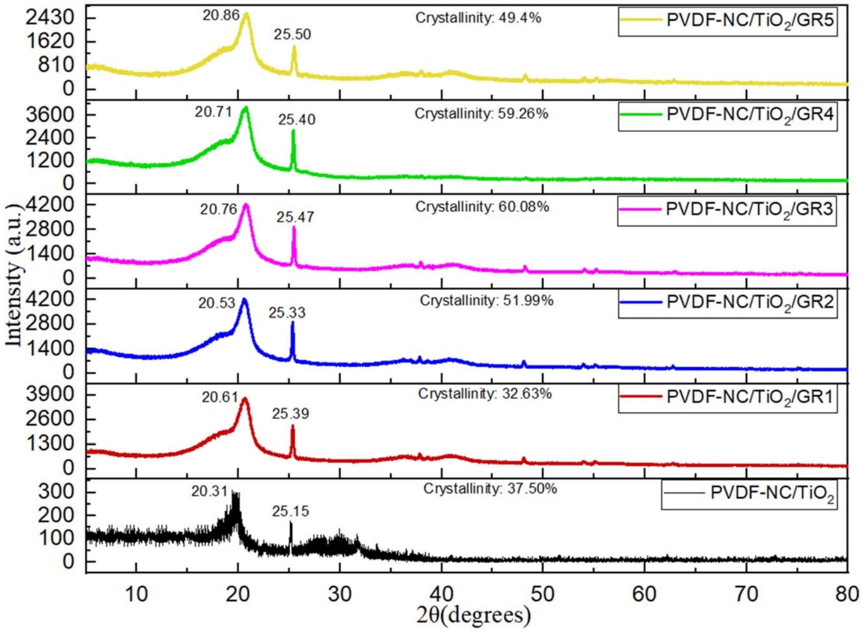

Fig. 2 The XRD patterns of the reference PVDF-NC/TiO_2 membrane and the graphene-incorporated PVDF-NC/TiO_2 membranes with varying graphene loading percentages.

groups in the PVDF-NC/TiO_2/GR membranes (S1–S5), as evidenced by the diminished C=O stretching vibration peak at approximately 2021 cm^{-1}, similar to the finding reported in the literature.[57] This peak typically attributed to carbonyl functionalities and its reduction suggests a low degree of surface oxidation in the GR-incorporated nanocomposite membrane. Consequently, the PVDF-NC/TiO_2/GR membranes exhibited a shift in surface chemistry toward a more carbon-dominated profile which likely reduced membrane hydrophilicity by weakening interactions with water molecules.[57]

3.2 Effect of GR incorporation on the crystalline structure of PVDF-NC/TiO_2 membranes

The XRD analysis presented in Fig. 2 was carried out to characterize the crystalline structure and phase composition of PVDF-NC/TiO_2 membranes incorporated with varying graphene loadings, in comparison to the control PVDF-NC/TiO_2 membrane without graphene. The analysis revealed significant diffraction peaks at approximately $2\theta = 20.31°$, 20.61°, 20.53°, 20.71° and 20.86° in all membrane profiles which indicated the existence of β phase. This finding aligned with previous work on PVDF/NC nanocomposite membranes, where a major diffraction peak at $2\theta = 20.43°$ was associated with the PVDF β phase.[29] In that study, the intensity of the β phase increased proportionally with higher NC loadings which suggested improved crystalline ordering. This improvement was due to the formation of hydrogen bonds between the hydroxyl groups of NC and the fluoropolymer chains of PVDF. Furthermore, the presence of NC also contributed significantly to the nucleation process by serving as an additional crystalline scaffold. Its high crystallinity and abundant surface hydroxyl groups enabled interfacial interactions and template-driven nucleation, complementing the role of GR. This was supported by several studies highlighting the role of NC in enhancing the crystallinity of various polymer matrices.[58–60] For instance, a study has reported that TEMPO-oxidized cellulose nanofibers (CNFs) facilitated the nucleation and crystal growth of ZIF-8 metal–organic frameworks (MOFs) aerogels through ionic and hydrogen bonding interactions which has resulted in significantly improved adsorption performance and structural stability.[61] This parallels with the NC function in the PVDF membranes, where it promoted β-phase formation and crystalline alignment.[31] Its uniform dispersion provided nucleation sites and improved chain packing, reinforcing the synergistic interaction with GR and contributing to the observed crystallite growth and structural refinement.

The β phase has been widely reported as the thermodynamically favoured crystalline phase in PVDF membranes, corresponding to the reflections from the (110) and (020) crystallographic planes.[62–64] Another diffraction peak observed at $2\theta = 25.15°$ represented the anatase phase of TiO_2 which was specifically associated with the (101) crystal plane.[29] Upon the incorporation of GR into the PVDF-NC/TiO_2 membrane, a slight increase in the intensity of this diffraction peak was observed as this peak position was also characteristic of natural graphite.[65] However, no significant differences in peak intensity and peak area were observed despite increased graphene loading percentages. To further evaluate the structural effects induced by GR incorporation, the average crystallite size of the membranes was calculated using the Scherrer equation, as shown in eqn (2). The control membrane (PVDF-NC/TiO_2) in the absence of GR, exhibited the smallest crystallite size of approximately 31.35 nm. This observation suggested limited nucleation and crystalline growth due to the lack of GR in the system.[66] Upon the incorporation of GR, a consistent increase in crystallite size was observed, with values of 36.93 nm (PVDF-NC/TiO_2/GR1), 36.97 nm (PVDF-NC/TiO_2/GR2), 36.97 nm (PVDF-NC/TiO_2/GR3), and 36.98 nm (PVDF-NC/TiO_2/GR4). These findings supported the role of GR as a heterogeneous nucleating agent that promoted enhanced polymer chain orientation and crystalline arrangement within the PVDF matrix.[67]

At a higher GR content, PVDF-NC/TiO_2/GR3 membrane displayed a slightly reduced crystallite size of approximately 36.26 nm. This reduction was likely due to nanoparticle agglomeration at elevated concentrations, which may have interfered with chain mobility and disrupted crystalline structure formation. Such behaviour was consistent with prior studies reporting that while nanofillers can promote crystallinity through nucleation, excessive loading may result in adverse effects on structural order (yan).

Additionally, the absence of a broad, noisy hump in the XRD profile of the PVDF-NC/TiO_2 membrane supported the assertion that incorporating GR nanoparticles improved the properties and functionality of the membrane.[68,69] A similar observation has been reported in the literature, indicating a correlation between polymer functionalization and crystallinity enhancement.[70] Such improvements were typically attributed to enhanced functional interactions and molecular ordering within the polymer matrix, resulting in a reduction of amorphous regions in PVDF-NC/TiO_2/GR nanocomposite membranes. The presence of NC further reinforced this ordering by reducing the disordered domains within the matrix, thereby complementing the function of GR in suppressing amorphous regions and promoting crystallinity.[71]

3.3 FESEM and EDX characterization of GR-induced structural and morphological changes in PVDF-NC/TiO_2 nanocomposite membranes

The FESEM images presented in Table 2 depict the top and cross-sectional morphologies of the control membrane (PVDF-NC/TiO_2) and its enhanced variants of graphene-incorporated membranes (PVDF-NC/TIO_2/GR). The detailed structural characteristics of these nanocomposite membranes were presented in Table 3. Based on the findings, the porosity of the membranes exhibited a nonlinear trend with increasing GR content. While PVDF-NC/TiO_2/GR1 and PVDF-NC/TiO_2/GR2 showed moderate porosity, a decline was observed in PVDF-NC/TiO_2/GR3, followed by a sharp increase in GR4 and GR5. This irregular pattern was not solely attributable to GR loading, but rather the result of complex physicochemical interactions among the materials during the membrane formation process. Notably, these effects appeared to be independent of viscosity

Table 2 Top surface and cross-sectional morphologies of all membranes

Nanocomposite membranes	Top surface morphology	Cross-sectional morphology
(a) PVDF-NC/TiO_2	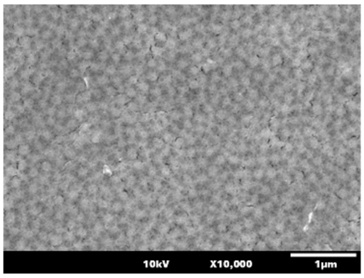	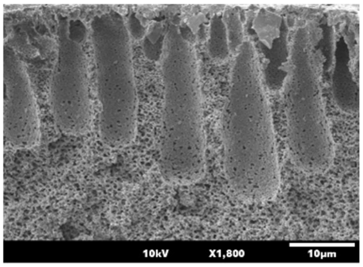
(b) PVDF-NC/TiO_2/GR1	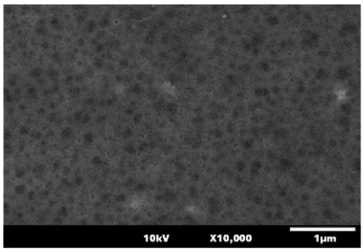	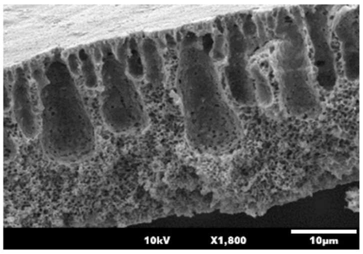
(c) PVDF-NC/TiO_2/GR2	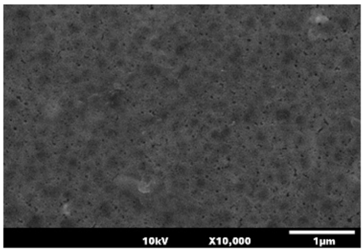	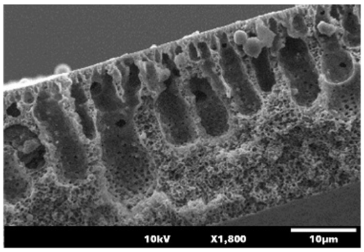
(d) PVDF-NC/TiO_2/GR3	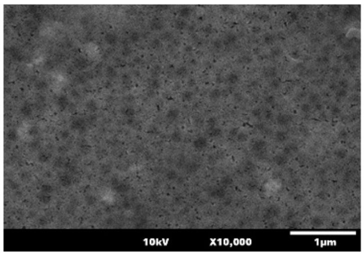	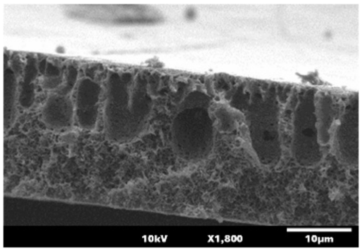
(e) PVDF-NC/TiO_2/GR4	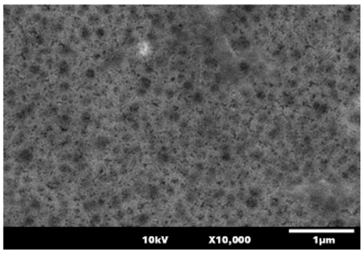	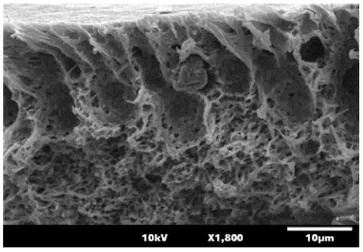
(f) PVDF-NC/TiO_2/GR5	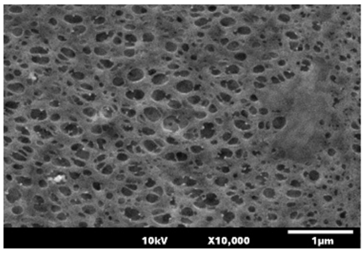	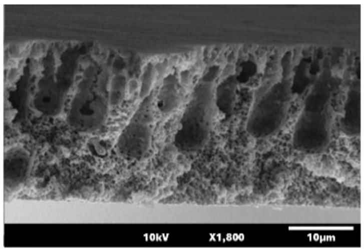

and were more closely related to thermodynamic factors, as reported in the literature.[72]

In particular, the reduced porosity observed in the PVDF-NC/TiO_2/GR3 membrane was attributed to the localised accumulation of GR which partially blocked nucleation sites for pore development. At this intermediate concentration, GR may have begun to agglomerate within confined regions that disrupted uniform dispersion and slowed the pore formation process. This structural compaction was evident in the cross-sectional FESEM image of PVDF-NC/TiO_2/GR3 which revealed a denser morphology compared to adjacent formulations. Furthermore, the presence of GR at this loading likely interfered with the hydrogen bonding network between NC and TiO_2, introducing competing interfacial interactions that diminished the thermodynamic instability typically promoting rapid demixing. Consequently, the solvent and non-solvent exchange slowed, impeding phase inversion and reducing porosity. Although partial agglomeration occurred in the PVDF-NC/TiO_2/GR3 membrane, it did not significantly compromise the interconnectivity of the pore network as the resulting porosity remained within a comparable range to values reported in previous studies. For example, polysulfone-based membrane incorporating 0.08 g of chitosan (PSU/CS-0.08) achieved an excellent 90% humic acid removal rate, despite having a developed pore size below 10 nm and a porosity range of only 60–70%.[73] This is further supported by the water flux permeation results shown in Fig. 3, where the PVDF-NC/TiO_2/GR3 membrane exhibited higher water flux compared to PVDF-NC/TiO_2/GR2 and PVDF-NC/TiO_2/GR1. This finding revealed that the interconnected pore structure in the membrane containing 0.6 wt% GR had remained sufficiently intact to allow effective water transport across the membrane.

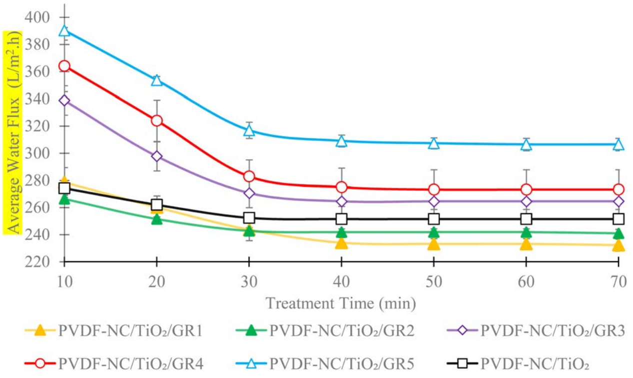

Fig. 3 Comparative water flux analysis of PVDF/NC/TiO_2/GR nanocomposite membranes with varying graphene loading percentages relative to the control PVDF/NC/TiO_2 membrane.

FESEM analysis revealed that all nanocomposite membranes exhibited irregular surface pores similar to the observations reported in prior work, despite the darker visual appearance due to GR incorporation.[29] At lower GR loadings, particularly in the range of 0.2–0.4 wt%, the top surfaces of the nanocomposite membranes exhibited a more refined and uniform pore distribution, resulting in modest mean pore size improvement compared to the control membrane. Specifically, the mean pore size increased from 4.89×10^{-3} µm for PVDF-NC/TiO_2 membrane to 4.99×10^{-3} µm and 5.19×10^{-3} µm for PVDF-NC/TiO_2/GR1 and PVDF-NC/TiO_2/GR2, respectively. This observation aligned with morphological findings from a previous study, where GR incorporation into pure PVDF membranes increased the number of surface pores and enlarged pore channels which significantly improved water permeation performance.[74] The formation of elongated channels facilitated directional solute transport across the membrane matrix further reinforcing the role of GR nanoparticles in facilitating selective separation through improved pore connectivity and induced structural anisotropy.[75] Additionally, porosity values remained consistent within the 77–79% range, indicating that low GR loadings induced controlled structural modifications without compromising membrane integrity. This maintained structural robustness contributed positively to both permeability and selectivity performance, allowing efficient dye removal while sustaining adequate water flux during operation.[76,77]

The surface morphological observations were further corroborated by cross-sectional morphology analyses which revealed a typical asymmetric membrane structure distinguished by a thin dense top layer supported by distinct finger-like void structures transitioning into a porous sponge-like sublayer.[14,29,78] Initially, the control membrane PVDF-NC/TiO_2 exhibited well-developed finger-like channels but lacked significant interconnected porosity. The incorporation of GR, even at low loadings of 0.2 wt%, initiated structural evolution towards improved porosity and the development of channel connectivity. The cross-sectional images of PVDF-NC/TiO_2/GR1 and PVDF-NC/TiO_2/GR2 revealed similar pore channel development, accompanied by the enhanced formation of vertically extended macrovoids with increasing GR content. This morphological improvement indicated that the inclusion of GR

Table 3 Structural characteristics of the nanocomposite membranes

Membrane	Mean pore size (µm)	Porosity (%)	Average thickness (µm)
PVDF-NC/TIO_2	$4.89 \times 10^{-3} \pm 0.06$	79.68 ± 0.65	44.3
PVDF-NC/TIO_2/GR1	$4.99 \times 10^{-3} \pm 0.12$	77.92 ± 2.48	41.3
PVDF-NC/TIO_2/GR2	$5.19 \times 10^{-3} \pm 0.06$	79.54 ± 0.54	46.3
PVDF-NC/TIO_2/GR3	$5.29 \times 10^{-3} \pm 0.31$	72.57 ± 1.43	44.3
PVDF-NC/TIO_2/GR4	$5.53 \times 10^{-3} \pm 0.22$	84.49 ± 0.71	46.3
PVDF-NC/TIO_2/GR5	$13.56 \times 10^{-3} \pm 0.06$	84.86 ± 0.97	46.6

as a functional additive promoted instantaneous demixing, accelerating phase separation and polymer precipitation during the phase inversion process.[79] The formation of numerous finger-like voids in the PVDF-NC/TiO_2/GR1 and PVDF-NC/TiO_2/GR2 nanocomposite membranes further supported this finding, indicating an improved demixing rate, particularly in terms of solvent–nonsolvent exchange kinetics during the phase inversion process that contributed to the formation of a well-developed porous structure.[80]

Meanwhile, the addition of GR up to 0.6 wt% in PVDF-NC/TiO_2/GR3 marked a transitional shift in pore development within the nanocomposite membrane morphology. The top surface of the membrane exhibited more prominent open pores while the formation of finger-like pore channels appeared shorter and broader, accompanied by a loosely packed sponge-like structure. This contrasted with the more defined and compact morphology observed in membranes with lower GR loadings. These changes were attributed to a reduced phase separation rate caused by increased GR content which altered the thermodynamic balance and slowed solvent exchange.[81,82] Notably, membranes with higher GR loadings (0.8–1.0 wt%) formed more prominent open pore structures as the viscosity of the casting dope solution slightly increased. This morphological transformation became evident in PVDF-NC/TiO_2/GR4, where the addition of 0.2 wt% GR to the PVDF-NC/TiO_2/GR3 formulation initiated the development of more abundant surface pores with slightly larger sizes, as confirmed by FESEM observations and the corresponding structural characteristics presented in Tables 2 and 3. However, a further increase in GR content beyond 0.8 wt% led to the formation of substantially larger pores as observed in the surface morphology of the PVDF-NC/TiO_2/GR5 membrane. This structural evolution resulted in increased surface porosity and a less compact morphology. The observed effect was primarily governed by thermodynamic instability surpassing kinetic influences which consequently influenced the performance of the membrane.[83] This observation was further supported by corresponding increases in mean pore size and porosity as presented in Table 3. The porosity percentages of the nanocomposite membrane increased from 84.49% for the membrane incorporating 0.8 wt% GR (PVDF-NC/TiO_2/GR4) to 84.86% for the membrane incorporating 1.0 wt% GR (PVDF-NC/TiO_2/GR5), simultaneously enhancing the mean pore size of the membrane from 5.53×10^{-3} μm to 13.56×10^{-3} μm.

Besides, the cross-sectional images of nanocomposite membrane containing 0.8–1.0 wt% GR loadings displayed a coarser and looser sponge-like structure compared to the others formulations. Previous studies have reported that excessive nanofiller loadings in membrane systems may disrupt thermodynamic stability during the phase inversion process.[83,84] Additionally, increased viscosity of the casting dope solution can delay the exchange between solvent and non-solvent which restricts mass transfer during membrane formation.[85–88] However, the present findings revealed a contrasting trend. In this study, the thermodynamic effect induced by the presence of hydrophilic nanofillers, particularly NC and TiO_2 appeared to have outweighed the kinetic resistance commonly associated with increased viscosity at higher GR loadings. The relatively low GR content in each membrane formulations (≤1.0 wt%) could only cause a slight increase in viscosity of the dope solution, which was insufficient to suppress the demixing process. A similar finding was also observed by other researchers, who stated that a slight increase in viscosity seldom exerted a significant influence on the phase inversion process.[89] Instead, the enhanced thermodynamic instability promoted by NC and TiO_2 facilitated rapid phase separation which resulted in the formation of larger surface pores and increased membrane porosity, as exhibited by PVDF-NC/TiO_2/GR5 membrane. The accelerated demixing process produced nanocomposite membranes with higher porosity and thinner selective top layers, a structural change that may enhance water permeability but potentially compromise dye rejection performance. As clearly presented in Table 3, the porosity of the nanocomposite membrane incorporating 0.8 wt% GR nanoparticles (PVDF-NC/TiO_2/GR4) showed a slight increase from 84.49% to 84.86% with the addition of 1.0 wt% GR (PVDF-NC/TiO_2/GR5) nanoparticles. Meanwhile, for membrane thickness, all nanocomposite membranes exhibited a typical and acceptable average thickness for asymmetric membranes which ranged between 41.3 μm and 46.6 μm.

As shown in the FESEM-EDX analysis tabulated in Table 4, the elemental distribution revealed successful incorporation of GR, with all GR-incorporated nanocomposite membranes showing a progressive increase in C percentages with values exceeding 53.57%, the baseline recorded in the control membrane. This observation confirmed the successful integration of GR as evidenced by the compositional changes attributed to the incremental addition of this carbon-rich nanomaterial into the membrane matrix. F was the second most abundant element detected across all nanocomposite membranes. This finding aligned with the intrinsic chemical structure of PVDF $(C_2H_2F_2)_n$, and was further supported by the characteristic C–F bond vibrations reported in the FTIR spectra of PVDF-based nanocomposite membranes.[29,31,90–93] However, the addition of GR led to a gradual reduction in F content which was attributed to the weakening of C–F bonds observed in the FTIR analysis. This weakening likely resulted from changes in surface chemistry associated with interactions between GR and the PVDF matrix during the membrane formation process. Such findings were in agreement with a previous study that reported higher GR content obstructed surface pores and modulated membrane surface properties.[65] As previously reported, the detection of Ti and O elements resulting from the inclusion of TiO_2 nanoparticles and nanocellulose has shown a reduction. This reduction was likely influenced by the diminished surface exposure of TiO_2 nanoparticles due to agglomeration as the GR content increased. As a result, possible agglomeration may have contributed to the reduction in Ti content from 2.90% in the control membrane to 1.83% in the membrane incorporating 1.0 wt% GR (PVDF-NC/TiO_2/GR5). Consequently, this led to uneven surface distribution of TiO_2 which consistent with the numerous white spots observed in the FESEM images as discussed in the preceding section.

Table 4 Elemental mapping and EDX spectral analysis of PVDF-NC/TIO$_2$ membranes with increasing GR content

Elemental distribution	EDX spectrum and quantitative elemental analysis

(a) PVDF-NC/TIO$_2$

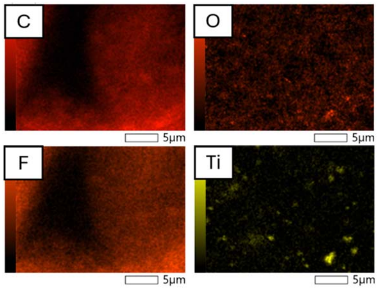

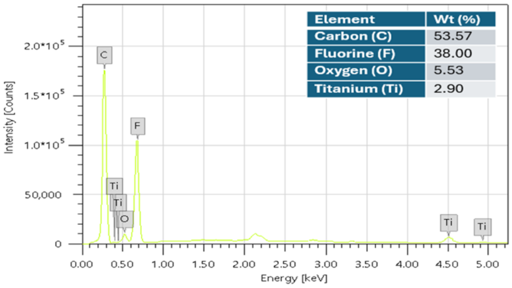

Element	Wt (%)
Carbon (C)	53.57
Fluorine (F)	38.00
Oxygen (O)	5.53
Titanium (Ti)	2.90

(b) PVDF-NC/TIO$_2$/GR1

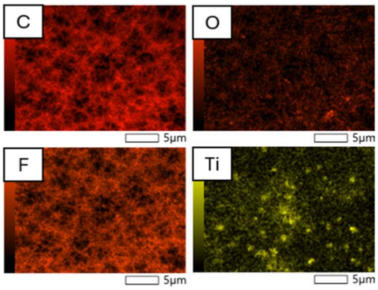

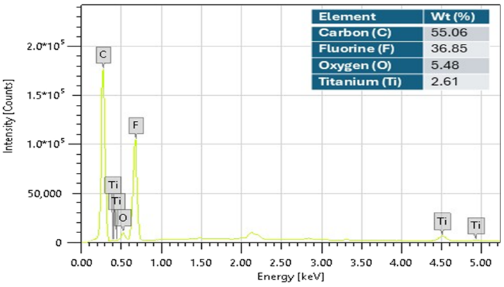

Element	Wt (%)
Carbon (C)	55.06
Fluorine (F)	36.85
Oxygen (O)	5.48
Titanium (Ti)	2.61

(c) PVDF-NC/TIO$_2$/GR2

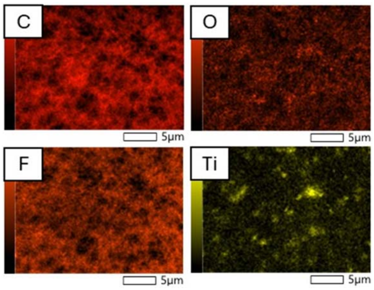

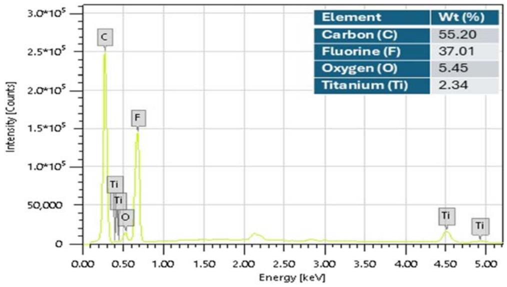

Element	Wt (%)
Carbon (C)	55.20
Fluorine (F)	37.01
Oxygen (O)	5.45
Titanium (Ti)	2.34

(d) PVDF-NC/TIO$_2$/GR3

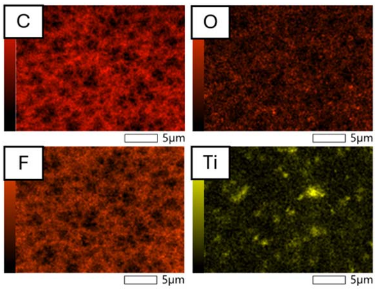

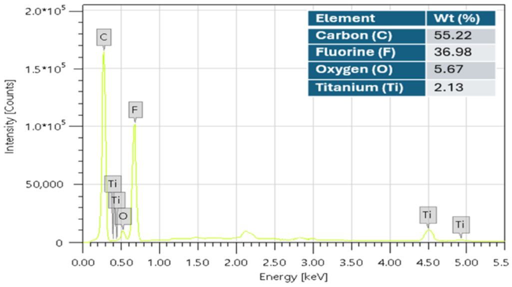

Element	Wt (%)
Carbon (C)	55.22
Fluorine (F)	36.98
Oxygen (O)	5.67
Titanium (Ti)	2.13

(e) PVDF-NC/TIO$_2$/GR4

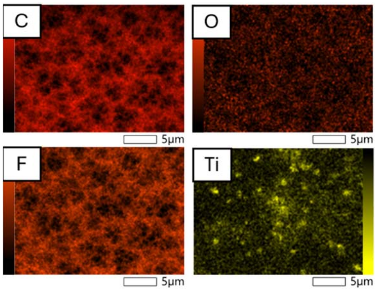

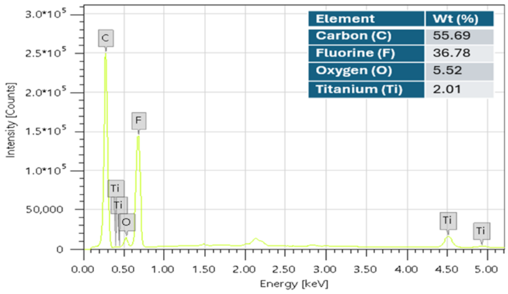

Element	Wt (%)
Carbon (C)	55.69
Fluorine (F)	36.78
Oxygen (O)	5.52
Titanium (Ti)	2.01

Table 4 (*Contd.*)

Elemental distribution	EDX spectrum and quantitative elemental analysis
(f) PVDF-NC/TIO_2/GR5	
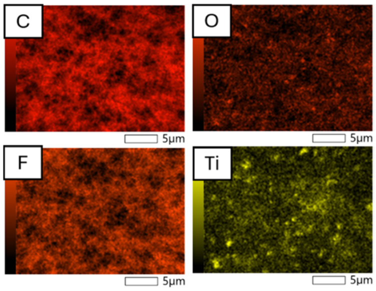	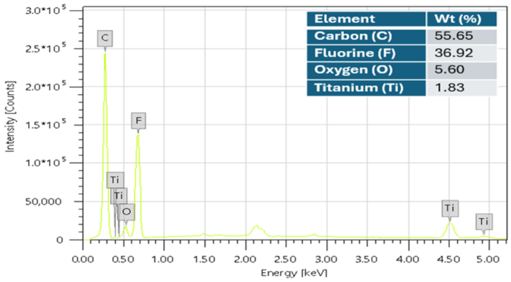 Element Wt (%) Carbon (C) 55.65 Fluorine (F) 36.92 Oxygen (O) 5.60 Titanium (Ti) 1.83

3.4 Evaluation of water permeation flux in GR-incorporated PVDF-NC/TiO_2 nanocomposite membranes

The water flux analysis presented in Fig. 3 was conducted to evaluate the impact of varying GR nanoparticle percentages on the permeability performance of PVDF/NC/TiO_2/GR nanocomposite membranes in comparison to a control membrane without GR. Based on the overall membrane performance, all nanocomposite membranes exhibited a steady water flux after 30 minutes of continuous filtration. At low GR loadings of 0.2–0.4 wt%, PVDF/NC/TiO_2/GR1 and PVDF/NC/TiO_2/GR2 demonstrated slightly reduced water permeation flux compared to the PVDF/NC/TiO_2 control membrane, despite having marginally enhanced mean pore sizes as presented in Table 3. In particular, PVDF/NC/TiO_2/GR1 recorded a stable flux of 234 L m^{-2} h^{-1} while PVDF/NC/TiO_2/GR2 achieved 241.92 L m^{-2} h^{-1}, both of which were lower than the 251.52 L m^{-2} h^{-1} recorded by the control membrane. This unexpected outcome may be attributed to several interconnected factors. Firstly, both PVDF/NC/TiO_2/GR1 and PVDF/NC/TiO_2/GR2 exhibited minimal improvements in porosity which likely had no significant impact on the overall water transport volume. A previous study similarly reported a comparison between two membranes with different porosity levels.[94] The study reported that a membrane with 90% porosity also recorded lower permeate than its lower-porosity membrane. Based on the literature, porosity does not necessarily equate to efficient water transport as the hydraulic performance of a membrane is primarily influenced by the interconnectivity of its pore network.[95] Based on the findings, the resulting flux was correlated with the development of smaller pore sizes and higher thermal conductivity, which possibly hindered water transport across the membrane. Additionally, the inherent hydrophobicity of GR nanoparticles may also have reduced surface wettability and water affinity, thereby affecting water permeation.[96] However, several studies have reported that a single layer of GR has a minimal influence on surface wettability, as it does not significantly alter the underlying composite substrate.[97,98] This phenomenon was due to the GR unique wettability characteristics, often known as wetting transparency. The researchers supported their findings using water contact angle (WCA) analysis which revealed values comparable to those of the substrate without GR. These findings suggested that low GR inclusion did not substantially modify the wettability of PVDF/NC/TiO_2/GR membranes. Nevertheless, as GR content increased, the composite substrate became increasingly hydrophobic as evidenced by rising WCA values reported in both experimental studies and molecular dynamics simulations.[99] Therefore, the hydrophobic behaviour imparted by GR was likely dependent on its dispersion, concentration, and interaction with the PVDF/NC/TiO_2 membrane matrix. Other important parameters that may have contributed to the low permeation volume of membranes incorporating 0.2–0.4 wt% include membrane thickness, structural density, and hydraulic resistance.[94,100]

On the other hand, the inclusion of GR nanoparticles beyond a threshold loading of 0.4 wt% resulted in a marked improvement in water permeation flux. This improvement was primarily attributed to significant morphological modifications, including the formation of numerous open surface pores with an increasing mean pore size and the development of highly interconnected pore networks as observed in nanocomposite membranes with higher GR content. Although partial agglomeration of GR was observed in PVDF-NC/TiO_2/GR3, it did not significantly hinder the formation of interconnected pores. Instead, the thermodynamic instability induced by the hydrophilic additives (NC and TiO_2) remained dominant during phase inversion which promoted the development of well-connected pores. As a result, PVDF-NC/TiO_2/GR3 exhibited higher water permeation flux compared to PVDF-NC/TiO_2/GR1 and PVDF-NC/TiO_2/GR2. This suggested that partial GR agglomeration may have coexisted with structural features favourable for water transport. These structural features not only facilitated efficient water transport but also contributed to fouling mitigation, as the degree of pore interconnectivity in membranes has been widely reported to influence fouling behaviour.[95] In general, the presence of additional interconnected pores with open surface structures aided in minimizing fouling during long-term membrane operation (Peng & Li, 2023). This effect was particularly evident in the nanocomposite membrane containing 0.6 wt% GR (PVDF/NC/TiO_2/GR3) which marked the threshold at which hydraulic performance began to improve. Despite some structural imperfections observed in the corresponding FESEM image, the membrane still demonstrated favourable pore connectivity and high permeability. At this loading, a notable increase in water flux was observed, reaching 270.74 L m^{-2} h^{-1} along with distinct morphological enhancements such as more open pores, enlarged mean pore size and improved pore interconnectivity as confirmed by FESEM analysis. This trend was further amplified in membranes incorporating higher GR contents. In contrast to previous studies which presented lower water permeation flux for all GR-free nanocomposite membranes, the present work demonstrated a substantial improvement in flux performance.[20,29] The PVDF-NC/TiO_2/GR5 membrane which contained the highest GR loading exhibited the highest water permeation flux among all tested membrane samples. This nanocomposite membrane achieved an initial flux of 390.39 L m^{-2} h^{-1} at 10 minutes, followed by a gradual decline to 307.42 L m^{-2} h^{-1} after 30 minutes. Similar to the performance demonstrated by PVDF-NC/TIO_2/GR4, the incorporation of 0.8% GR loadings yielded a flux of 364.19 L m^{-2} h^{-1} which stabilized at a constant value of 273.36 L m^{-2} h^{-1}. These results aligned with the findings from the earlier reports that emphasized the advantages of the synergistic effect of GR in modifying both the structural and surface properties of the PVDF membrane.[101–103] Membranes with highly interconnected pores allowed fluid to bypass or flow beneath areas of surface blockage, thereby reducing the adverse effects of localized fouling on overall permeate flux.[98] Furthermore, such pore structures contributed to enhanced membrane stability during extended operation by delaying the onset of fouling and enabling more effective removal of foulants during cleaning cycles.[104] In addition, these structural modifications significantly enhanced water transport across the nanocomposite membrane by reducing hydraulic resistance.

3.5 Evaluation of MB dye rejection flux, photocatalytic efficiency and their relationship to the fouling recovery ratio of nanocomposite membranes

Comparative analyses of PVDF/NC/TiO_2 and PVDF/NC/TiO_2/GR nanocomposite membranes were conducted to evaluate their performance in the separation of MB dye comprehensively. Each sample was tested in quintuplicate with the resulting average values used to construct the trend lines presented in Fig. 4 and 5. Based on the analyses, although membranes with 0.2–0.4 wt% GR loadings exhibited lower flux compared to the control membrane, their dye rejection performance remained high and consistent with values reported in previous studies. Even at a minimal GR loading of 0.2 wt%, the PVDF-NC/TiO_2/GR1 nanocomposite membrane maintained a consistently high dye removal efficiency of 93–94% throughout the operational period with only a slight decline observed. Although the initial rejection flux of this membrane was lower than those PVDF-NC/TIO_2/GR2 and the control membrane, the PVDF-NC/TiO_2/GR1 membrane exhibited stable operation performance in both flux and rejection over time.

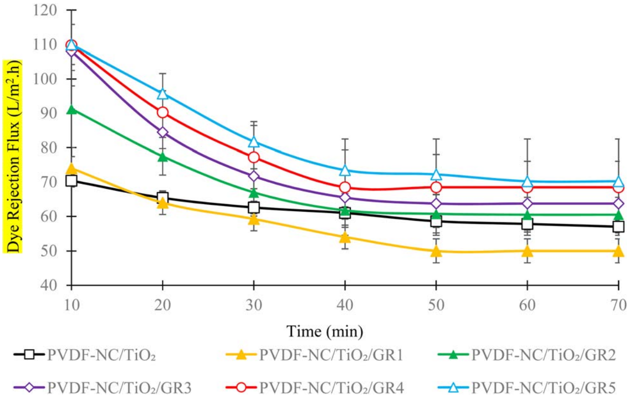

Fig. 4 Comparative dye rejection analysis of PVDF/NC/TiO_2/GR nanocomposite membranes with varying graphene loading percentages relative to the control PVDF/NC/TiO_2 membrane.

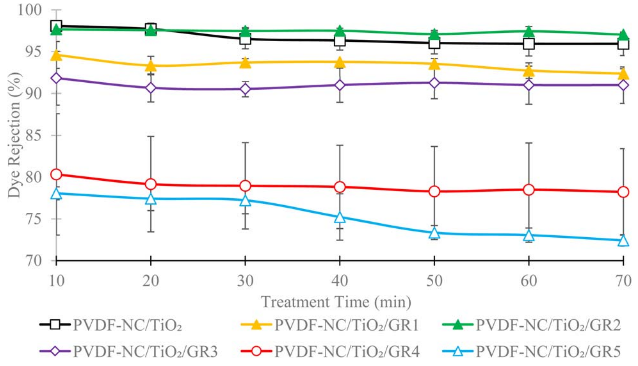

Fig. 5 Analysis of MB dye removal percentages of PVDF/NC/TiO_2/GR nanocomposite membranes with varying graphene loading percentages relative to the control PVDF/NC/TiO_2 membrane.

Increasing the GR loading to 0.4 wt% significantly improved the performance of the membrane. The PVDF-NC/TiO_2/GR2 membrane achieved a high dye removal efficiency of 97% after 70 minutes of continuous treatment, outperforming both the control and 0.2 wt% GR membranes. Besides, PVDF-NC/TiO_2/GR2 also recorded a slightly higher initial rejection flux of 91.25 L m^{-2} h^{-1} in the first 10 minutes and stabilized at a value of 60.5 L m^{-2} h^{-1}. In contrast, the control membrane displayed an initial rejection flux of 70.4 L m^{-2} h^{-1}, which gradually declined to 57 L m^{-2} h^{-1} due to progressive pore blockage. These findings confirmed the beneficial role of GR in enhancing dye rejection efficiency and membrane durability even under continuous operation. The results were in agreement with previous studies. For instance, a study reported that GR-incorporated membranes achieved cationic dye removal efficiencies ranging from 97% to 98% due to the enhanced electrostatic adsorption, molecular sieving effects, and π–π interactions.[105] The incorporation of GR was also found to

Table 5 Summary of performance comparison among various mixed membranes for dye separation[a]

Membranes	Type of filler	Water flux permeation (L m^{-2} h^{-1})	Type of dye	Dye rejection (%)	FRR (%)	References
PVDF/GO/PVP/PEG	GO	>110	MB	83.5	—	80
PVDF/GO/TiO_2	GO, TiO_2	87.32	MB	92.63	100	109
PES/GO/TiO_2		87.72		86.58	—	
PVDF/GO with rGO layer	GO, rGO	1690	Cationic & anionic dye	97–98	—	105
CA/coated rGO layer membrane	rGO	26.5	Aniline blue	72	70	110
DACNC/Ag/EGO	EGO, Ag NPs	69.03	MB	94	80.4	111
PES/APTS-GO/ PVP mixed membrane	APTS-GO	9.9	Twilight yellow, acridine orange	97.4, 96.5	52	112
PES/GO/PVP	GO	23.32	Rhodamine B	91.96–96.92	55.99	113
Functionalization of DES/GO membrane	GO	124.8	Congo red, methyle blue, evan blue, direct blue	99.4, 96.7, 98.5, 99.3	74–100	114
GO/PES membrane	GO (0.5 wt%)	116.5	Acid black 210, rose bengal	98.9–99	—	115
MOF@chitosan-GO	Chitosan, GO	34.5	Congo red	95.6	77.5	116
PVDF-NC/TiO_2/GR3	NC, TiO_2, GR	270.74	MB	91	83	Present study

[a] Shear-aligned graphene oxide@PVDF (SAGO@PVDF), cellulose acetate (CA), polyethersulfone (PES), 3-aminopropyltriethoxysilane functionalized graphene oxide (APTS-GO), ethylenediamine-functionalized GO (EGO), silver nanoparticles (Ag NPs), polyvinylpyrrolidone (PVP), polyethylene glycol (PEG), double aldehyde cellulose nanocrystals (DACNC), deep eutectic solvent (DES).

enhance the availability of active sites and suppress fouling, both of which were critical factors in sustaining long-term membrane performance.[106,107] When compared to other modified GR-based membranes, the result from the present study appeared highly competitive. As an example, a PVDF membrane embedded with GO achieved a MB removal efficiency of 83.5% under visible light irradiation.[80] Another study showed that the incorporation of synergistic TiO_2 and rGO nanoparticles into a PVDF membrane resulted in a MB dye removal efficiency of 92% along with a FRR of 95.3%.[108] Additionally, a separate study reported that incorporating hybrid additives such as TiO_2 and GO into a PVDF matrix produced a highly porous membrane that achieved 92.63% dye rejection and a flux recovery ratio approaching 100%.[109] To further contextualize the performance of the fabricated PVDF-NC/TiO_2/GR membranes, a comparison with other reported mixed matrix membranes used for dye removal has been summarized in Table 5.

The superior performance of the PVDF-NC/TiO_2/GR membrane underscored the advantages of incorporating pristine GR over its oxidized counterparts, in particular GO and rGO. While GO and rGO promoted an abundance of oxygen-containing functional groups (hydroxyl, carbonyl, epoxy), their tendency to aggregate under certain conditions was known to hinder membrane performance.[117,118] In contrast, the inclusion of GR preserved membrane integrity while enabling improved conductivity, surface area and compatibility with other additives.[119] A previous analysis reported a maximum dye removal rate of 98% for the PVDF-NC/TiO_2 membrane (control membrane, S0 in Fig. 5); however, this efficiency gradually decreased to 95% during continuous operation as membrane fouling had commenced.[29] In the present study, the enhanced stability and sustained performance of the PVDF-NC/TiO_2/GR membrane highlighted the synergistic effect of GR with NC and TiO_2. This combination proved effective in mitigating fouling tendencies and improving membrane durability under prolonged operation. Owing to its exceptional properties, the presence of GR nanoparticles in the nanocomposite membrane enhanced the pore size and introduced additional active sites within the membrane matrix which improved membrane separation performance and overall efficiency. GR is characterised by a high surface area of approximately 2630 m^2 g^{-1}, which offers numerous active sites for adsorption, thereby allowing for a significant improvement in pollutant removal capacity for wastewater treatment.[120,121] Meanwhile, the incorporation of 0.6 wt% GR into the membrane system resulted in a high initial dye rejection flux of 108 L m^{-2} h^{-1}, which gradually declined to 60.5 L m^{-2} h^{-1}. Despite this reduction, the membrane maintained an impressive dye removal efficiency of 91%.

However, excessive GR loadings of 0.8–1.0 wt% adversely affected dye separation efficiency as evidenced by the large gaps observed in the corresponding membrane samples displayed in Fig. 5. This reduction was attributed to structural changes apparent in the FESEM images, where high GR concentrations induced the formation of defects, oversized surface pores and pore blockage. Many studies reported that an enhancement in porosity can lead to outstanding permeation flux, however, this often compromises membrane selectivity in removing foulants during treatment due to the development of larger pore sizes.[122–125] These changes disrupted membrane uniformity, restricted access to active adsorption sites and potentially contributed to leakage. In addition to morphological changes, performance deterioration at higher GR loadings also plausibly contributed to the changes in membrane surface wettability as previously discussed. Although WCA analysis could not be performed due to equipment constraints, prior studies have reported that the absence of oxygen-functional groups on GR nanoparticles reduced the surface hydrophilicity of the fabricated membranes.[126–128] As an example, the inclusion of infused graphene (G) into PVDF to form PVDF/G composites significantly increased surface hydrophobicity with WCA increase of approximately 20° compared to the pristine PVDF, accompanied by an enhanced in surface roughness.[129] A similar study reported that the blending of graphene (GE) with PVDF formed composite membrane (PVDF)/GE with a surface WCA of 124.6° also indicating pronounced hydrophobic characteristics.[130] Such result represented a substantial increase in WCA compared to the composite membrane without GR (GE-0).

In the context of the present study, increasing GR loading appeared to have imparted hydrophobic characteristics to the surface of the PVDF-NC/TiO_2/GR membrane which consequently diminished the formation of a hydration layer that typically resisted foulant adhesion. This shift in surface wettability may have partially contributed to the reduced FRR and MB dye removal performance observed in PVDF-NC/TiO_2/GR4 and PVDF-NC/TiO_2/GR5 samples. This finding aligned with previous reports on hydrophobic membranes, which commonly exhibited lower flux, higher fouling susceptibility and reduced separation efficiency.[131,132] Supporting this, a study that compared the separation performance of PVDF-based membranes with two different surface wettabilities found that hydrophilic membranes exhibited a separation flux of 22.88 L m^{-2} h^{-1} with an efficiency of 93.35% for oil-in-water emulsions, while the hydrophobic membranes achieved a lower flux of 17.45 L m^{-2} h^{-1} and 91.47% effectiveness.[133] Although hydrophobic membranes have been reported in the literature to offer advantages in specific niche applications, such benefits were not observed in the present study.

Experimental results further confirmed the negative impact of excessive GR content. The PVDF-NC/TiO_2/GR4 exhibited an initial flux of 109.75 L m^{-2} h^{-1} that stabilized at 68.5 L m^{-2} h^{-1}, but its dye removal efficiency ranged only between 78% to 80%. Among all membrane samples, PVDF-NC/TiO_2/GR5 showed the highest initial dye rejection flux of 110 L m^{-2} h^{-1} during the first 10 minutes. However, its dye rejection flux began to reduce after 30 minutes of continuous treatment. Despite achieving the highest rejection flux, the PVDF-NC/TiO_2/GR5 membrane recorded the lowest dye removal efficiency, particularly 77% during the first 30 minutes which further declined to 72% in the subsequent treatment time. This reduction in performance was due to the development of larger pore diameters as shown by the increased mean pore sizes presented in Table 4. The enlargement of pore size reduced the ability of the membrane to effectively retain dye molecules, consequently leading to diminished size exclusion capability and lower dye separation performance due to increased dye permeation through the membrane.

Extending the prior analysis of dye separation efficiency, this section examined the photocatalytic performance and antifouling behaviour of the nanocomposite membranes to provide deeper insight into their self-cleaning potential under UV-light irradiation. The visual comparisons of PVDF-NC/TiO_2 and PVDF-NC/TiO_2/GR membranes before and after photocatalytic treatment have been presented in Table 6, while the corresponding quantitative performance has been illustrated in Fig. 7. As reported in previous study, the incorporation of TiO_2 was identified as an effective approach to reduce the frequency of membrane backwashing which were often associated with high operational costs and time-consuming maintenance.[29] In the present study, GR was incorporated to further improve the photocatalytic efficiency of TiO_2 within the membrane matrix, aiming to enhance antifouling performance. This reflected the growing research interest in leveraging the advancement of TiO_2-based nanocomposites for multifunctional membrane applications.[134–136] During photodegradation under visible UV-light irradiation, TiO_2 absorbed photons with energy ($h\nu$) equivalent to or higher than its bandgap ($E_g = 3.2$ eV), resulting in the excitation of electrons from the valence band (VB) to the conduction band (CB).[137] The excitation generated positively charged vacancies or holes in the VB. In typical semiconductor-based photocatalysis, the rapid recombination of photogenerated electron–hole (e^- and h^+) pairs severely limits photocatalytic efficiency.[138] Incorporating GR addressed this limitation by serving as an effective electron acceptor and transport medium which enhanced charge separation and prolonged the lifetime of reactive species essential for photocatalytic reactions. GR was widely recognised as an excellent electron acceptor that enhanced the overall photocatalytic activity of TiO_2. According to the literature, this improvement was attributed to the exceptionally low charge transfer resistance which facilitated more efficient electron mobility across the TiO_2-GR interface.[138,139] This analysis was supported by previous studies that reported the incorporation of supplementary inorganic additives led to the development of hybrid membranes with enhanced photocatalytic activity, owing to the more pronounced effect of nanoparticles in driving the photodegradation process.[84,140–142] Such observation was clearly reflected in the membrane performance observed in the present study.

At 0.2 wt% GR loading, a slightly lower flux recovery ratio (FRR) of 91% was observed as indicated by the trend line in Fig. 6, which still demonstrated considerable reusability potential. In comparison, the membrane with 0.4 wt% GR loadings achieved the highest FRR of 98% highlighting superior self-cleaning ability and fouling resistance. Membrane with highly interconnected pores allowed fluid to bypass or flow beneath areas of surface blockage, thereby reducing the adverse effects of localized fouling on overall permeate flux.[98] However, further increases in GR loading led to a gradual decline in FRR values, with 83% recorded for PVDF-NC/TiO_2/GR3, 76% for PVDF-NC/TiO_2/GR4 and 71% for PVDF-NC/TiO_2/GR5, the lowest among all. These findings aligned with previous analysis which reported that excessive GR content could adversely affect photocatalytic efficiency due to nanoparticles agglomeration and the subsequent blockage of active sites.[143]

NC, another nanofiller included in the membrane formulation, also played a significant role in enhancing the antifouling behaviour of the PVDF-NC/TiO_2/GR system. The porous structure of NC offered numerous voids that expanded the active surface area available for the adhesion and physical entrapment

Table 6 Visual comparison of nanocomposite membrane samples before and after photocatalytic treatment with corresponding dye collection over time

Membranes	Pre-photocatalytic treatment	Dye collection over treatment time	Post-photocatalytic treatment
PVDF-NC/TIO_2	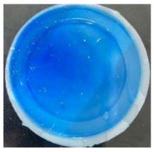	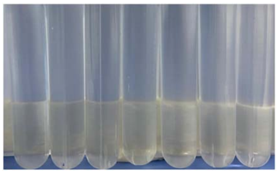	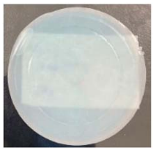
PVDF-NC/TIO_2/GR1			
PVDF-NC/TIO_2/GR2	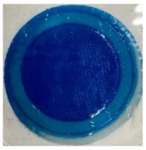	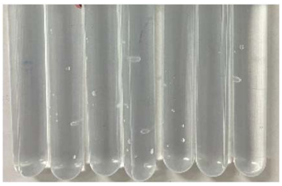	
PVDF-NC/TIO_2/GR3			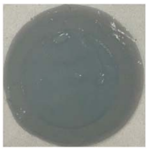
PVDF-NC/TIO_2/GR4			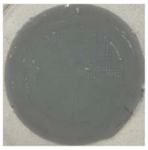
PVDF-NC/TIO_2/GR5	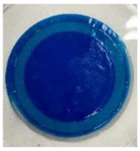		

of MB foulants. Besides, a key function of NC was its ability to form hydrogen bonds with surrounding water molecules, owing to the abundance of hydroxyl groups present on its surface.[144,145] This hydrogen bonding interaction has been reported to support the formation of a stable hydration layer on the membrane surface.[146,147] Such a hydration layer acted as an effective barrier against strong foulant adhesion as well as reduced the likelihood of irreversible fouling. Moreover, this hydration barrier complemented the electrostatic adsorption process by ensuring that even after MB foulants were attracted to the surface, their strong adhesion was minimised which allowed subsequent photocatalytic degradation by TiO_2 and GR to proceed more efficiently. This finding highlighted why 4 wt% NC loading was identified as optimal, as it not only provided sufficient hydrogen bonding capacity through abundant hydroxyl groups but also facilitated efficient solvent and non-solvent exchange during the phase inversion process.[14] As a result, the FESEM images from the earlier work revealed well-defined finger-like pores and improved membrane porosity which led to improved permeability and fouling resistance of the PVDF-NC membrane. However, the antifouling benefits imparted by NC were found to be partially compromised at higher GR loadings. The findings of the present study showed that increasing GR content imparted hydrophobic

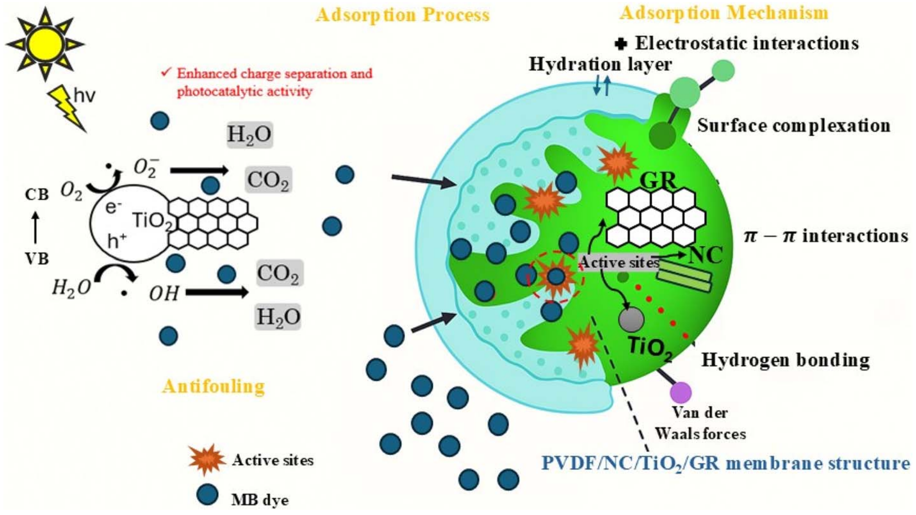

Fig. 6 Schematic illustration of antifouling, adsorption and photocatalytic mechanisms of the PVDF–NC/TiO_2/GR nanocomposite membrane for MB dye removal.

characteristics to the membrane surface which suppressed the formation of the layer essential for resisting MB foulant attachment.

In parallel, electrostatic interactions between MB and the membrane surface also significantly influenced separation performance. Several investigations have shown that altering the surface charge of membranes, either to improve positive or negative surface was effective in mitigating fouling tendencies.[148,149] In this study, MB, a cationic dye, exhibited adsorption behaviour that was strongly governed by the surface charge of the PVDF-NC/TiO_2/GR membrane. Although no specific data on the zeta potential were available in the present study, prior literature has reported that both pristine PVDF and NC exhibited a negatively charged surface in an aqueous environment. According to the literature, the zeta potential of a pristine PVDF membrane ranged between −9 to −23.2 mV, attributed to the presence of C–F moieties.[150] The presence of 4 wt% NC likely intensified the negatively charged surface of the PVDF-NC/TiO_2/GR membrane, as supported by previous findings in which sulfuric acid-hydrolysed cellulose nanocrystals (CNC) exhibited zeta potentials as low as −37.1 mV.[151] The negatively charged membrane surface facilitated the electrostatic attraction of cationic MB molecules and initiated dye adsorption. While electrostatic interactions enhanced dye adsorption, prolonged exposure could have resulted in surface fouling due to MB accumulation. To address this, the integrated photocatalytic activity of TiO_2 and GR played a synergistic role in mitigating this issue.

Additionally, it was reported that excessive GR in TiO_2-based systems increased light adsorption by GR, thereby restricting photon availability for TiO_2 activation and reducing the relative proportion of active TiO_2 sites responsible for radical generation. Such factors subsequently diminished the photocatalytic and antifouling performance of the PVDF-NC/TiO_2/GR. This emphasized the importance of optimising GR content to achieve a balance between enhanced photocatalytic function and structural integrity for efficient membrane operation. The overall mechanisms governing antifouling and adsorption in the PVDF–NC/TiO_2/GR membrane system were illustrated in the schematic diagram presented in Fig. 6 which was linked to the membrane performance results shown in Table 6 and represented the adsorption, photocatalytic and antifouling outcomes.

3.6 Adsorption isotherm modelling and surface interaction behaviour of nanocomposite membranes

To evaluate the adsorption behaviour of MB dye molecules onto the PVDF-NC/TiO_2/GR membranes and their interaction with active sites, equilibrium adsorption isotherm analysis was conducted at 25 °C. The experimental data were evaluated using both the Langmuir and Freundlich models, with the corresponding parameters summarized in Table 7. Among these, the Langmuir model provided the best fit to the experimental data as shown in Fig. 7, which was evidenced by its higher linear correlation coefficient (R^2) ranging between 0.85 to 0.99. In comparison, the Freundlich model which commonly used to describe heterogeneous surface adsorption exhibited considerably lower R^2 values. These results confirmed that the MB dye molecules predominantly formed a monolayer coverage on uniformly distributed active sites which were consistent with the assumption of the Langmuir model. In line with the present observation, several studies have reported similar findings. For instance, a study reported that the equilibrium data for MB dye adsorption onto both Algerian kaolinite (DD3) and sulfuric acid-treated DD3 exhibited an excellent fit with the Langmuir model compared to the Freundlich model.[152] The Langmuir model achieved remarkably high R^2 values of 0.999 for both DD3 and treated-DD3, whereas the Freundlich model presented comparatively lower R^2 values of 0.937 and 0.866. Similarly, another study reported that the adsorption behaviour of MB dye onto a polyethylene (PE) matrix embedded with calcium carbonate ($CaCO_3$) mineral filler also followed the Langmuir

Table 7 Langmuir and Freundlich isotherm parameters for MB dye adsorption onto active sites

	Langmuir model			Freundlich model		
Membranes	Q_{max} (mg g^{-1})	K_L (L mg^{-1})	R^2	K_F (L mg^{-1})	n	R^2
PVDF-NC/TIO$_2$	0.996	478.000	0.97	−7.538	−4.350	0.010
PVDF-NC/TIO$_2$/GR1	0.497	42.874	0.99	0.126	−1.486	0.949
PVDF-NC/TIO$_2$/GR2	0.548	100.796	0.85	0.110	−1.733	0.345
PVDF-NC/TIO$_2$/GR3	1.866	72.405	0.96	1.693	45.045	0.155
PVDF-NC/TIO$_2$/GR4	0.567	11.988	0.92	−0.072	−80.645	0.104
PVDF-NC/TIO$_2$/GR5	0.275	5.302	0.97	−0.151	−50.000	0.375

isotherm which exhibited the highest R^2 values compared to the Freundlich, Temkin and Dubinin–Radushkevich models.[153]

These comparative findings further validated the applicability of the Langmuir model to the current PVDF-NC/TiO$_2$/GR membrane system. According to the Langmuir theory, adsorption was assumed to occur as a monolayer on a surface containing a finite number of energetically identical active sites, where each site could accommodate only one MB dye molecule without further interactions between adsorbed species.[154,155] This model allowed accurate determination of the maximum MB dye adsorption capacity (Q_{max}), the Langmuir adsorption affinity constant (K_L) and the correlation coefficient (R^2), all of which aligned well with the membrane morphology and surface activity.

As displayed in Table 7, the control membrane (PVDF-NC/TiO$_2$) recorded the highest K_L value of 478 L mg^{-1}, which was

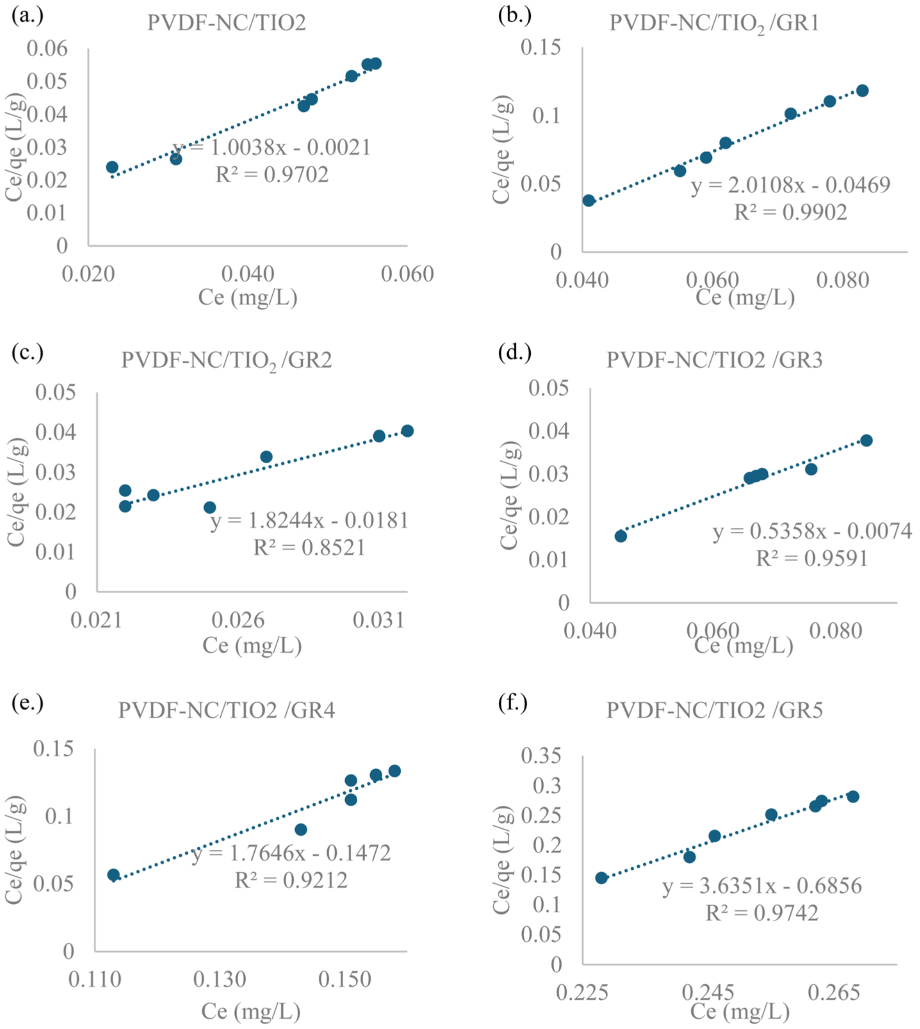

Fig. 7 Linearized Langmuir isotherm plots for MB dye adsorption onto (a) PVDF-NC/TiO$_2$, (b) PVDF-NC/TiO$_2$/GR1, (c) PVDF-NC/TiO$_2$/GR2, (d) PVDF-NC/TiO$_2$/GR3, (e) PVDF-NC/TiO$_2$/GR4, (f) PVDF-NC/TiO$_2$/GR5 nanocomposite membranes at 25 °C.

approximately 6.6 times greater than that of the PVDF-NC/TiO_2/GR3 membrane. This pronounced K_L value indicated an exceptionally strong binding affinity between MB dye molecules and the available active sites on the PVDF-NC/TiO_2 membrane. Such high affinity suggested intense adsorbate to adsorbent binding interactions that may have deviated from the ideal Langmuir assumption of monolayer adsorption on uniform and independent sites, particularly under conditions of high surface reactivity and site-specific binding. As reported by a researcher in the context of strong energy regimes, the Langmuir model predicted lower pollutant occupancy despite high binding affinity due to the increased likelihood of multiple-site interactions.[156] In the present study, the applicability of the Langmuir model was further supported by the high R^2 value of 0.97 observed for the control membrane in contrast to the extremely low R^2 value of 0.01 observed using the Freundlich model. This significant disparity confirmed that the adsorption behaviour was better represented by the Langmuir model, implying monolayer adsorption on a homogeneous surface.

This behaviour was likely influenced by the absence of GR nanoparticles in the control membrane, which preserved the accessibility and chemical integrity of the TiO_2, NC and PVDF active sites. This configuration allowed stronger electrostatic interactions between the cationic MB dye molecules and the membrane surface. Additionally, the absence of GR allowed greater exposure of fluorine-containing groups on the PVDF surface, thereby increasing surface polarity due to the inherent electronegativity of fluorine atoms.[157] This improved polarity further strengthened the surface interaction, contributing to the high dye affinity and enhanced antifouling performance observed in the respective membrane.[158] Such structural and chemical characteristics, including energetically equivalent active sites and one-to-one binding interactions were consistent with the assumptions of the Langmuir isotherm model. However, despite the strong affinity demonstrated by the control membrane, it exhibited a slightly lower Q_{max} of 0.996 mg g^{-1} compared to the membrane incorporated 0.6 wt% GR, which achieved 1.866 mg g^{-1}. This result indicated that while the control membrane offered highly favourable surface interactions, the presence of GR nanoparticles in the membrane system improved the overall dye uptake.

One of the primary factors contributing to the higher Q_{max} observed in PVDF-NC/TiO_2/GR3 was the presence of numerous open surface pores and the optimal pore size enlargement which collectively improved the accessibility of MB dye molecules to the active sites of the membrane. This structural feature reduced mass transport resistance and enabled molecular diffusion which allowed effective dye adsorption. A similar observation was reported in a study where the incorporation of Fe_3O_4 into chitosan-based nanocomposites improved surface accessibility and provided additional adsorption sites for dye molecules.[159] Another study reported that the inclusion of onion-derived carbon nanoparticles into polysulfone (PSU) membrane produced a porous network that matched the molecular size of MB dye.[160] Such structural features promoted rapid dye diffusion and adsorption, aligning with the pore-driven mechanism observed in PVDF-NC/TiO_2/GR3. Furthermore, when comparing maximum adsorption capacities with findings from other studies, the PVDF-NC/TiO_2/GR3 membrane developed in this work demonstrated superior adsorption performance. Specifically, it outperformed a previously reported 3 mg rGO/PVDF membrane which reported a Q_{max} of 1.287 mg g^{-1} based on the Langmuir model with an R^2 value of 0.985, indicating favorable one-to-one binding interactions.[161] In contrast, the unmodified 5 mg rGO/PVDF membrane exhibited a much lower Q_{max} of 0.416 mg g^{-1} and a poor model fit, with an R^2 value of only 0.505 for Rhodamine dye adsorption. This improvement was associated with the increased surface area and the availability of more accessible active sites resulting from the synergistic integration of NC, TiO_2 and GR which collectively facilitated greater dye capture.

At lower range of GR loadings, particularly 0.2–0.4 wt%, PVDF-NC/TiO_2/GR1 and PVDF-NC/TiO_2/GR2 membranes showed moderate Q_{max} values of 0.497 and 0.548 mg g^{-1}. However, the K_L values exhibited a relatively high amount of 42.874 L mg^{-1} and 100.796 L mg^{-1}, respectively. These values reflected the improved dye-surface affinity due to better porosity and macrovoid formation, despite the limited available surface for maximum adsorption to take place. Beyond 0.6 wt% GR loadings, the adsorption performance of the membrane started to reduce significantly. In particular, the PVDF-NC/TiO_2/GR4 and PVDF-NC/TiO_2/GR5 membranes exhibited notably lower Q_{max} values of 0.567 and 0.275 mg g^{-1}, alongside decreased K_L values of 11.988 L mg^{-1} and 5.302 L mg^{-1}. This reduction was attributed to TiO_2 nanoparticle agglomeration and partial pore blockage at high GR loadings which restricted MB dye access to active sites and disrupted the uniformity of the adsorption surfaces. This interpretation was further supported by morphological observations which revealed excessive pore enlargement and reduced membrane compactness, both of which affected selective adsorption performance.

4 Conclusion

The development of a multifunctional PVDF-based nanocomposite membrane reinforced with bamboo-derived NC, TiO_2, and pristine GR offers a highly effective method for treating MB-contaminated industrial wastewater. In this study, the membrane was fabricated using a modified phase inversion method to ensure uniform nanofiller dispersion and improved structural integrity. FTIR analysis confirmed the successful integration of GR through attenuation of semi-ionic C–F bonds and the emergence of C=C bands. Additionally, XRD results showed that the membranes retained their β-phase crystallinity with slight increases in peak intensity attributed to the presence of GR. This retention of the β-phase has been found to be significant, as it represents the most stable and polar crystalline form of PVDF by contributing to enhanced mechanical strength, thermal stability, and long-term membrane performance. Moreover, FESEM and EDX analyses revealed enhanced pore morphology and increased carbon content, with pore size rising from 4.89×10^{-3} μm to 13.56×10^{-3} μm and porosity from 79.68% to 84.86%. The membrane with 1.0 wt% graphene achieved the highest water flux at 307.42 L m^{-2} h^{-1} after 30 minutes of treatment stabilization, while 0.4 wt% GR delivered optimal dye rejection efficiency of 97%. The similar membrane also exhibited strong antifouling performance by recording a flux recovery ratio of 98% after UV treatment. This study has also found that Langmuir isotherm modeling best described the adsorption behavior which indicated monolayer uptake with high correlation ($R^2 = 0.85–0.99$), where $Q_{\max}$ reached 1.866 mg g^{-1} for the 0.6 wt% GR membrane and K_L peaked at 478 L mg^{-1} for the control membrane. Nonetheless, Freundlich modeling showed lower average correlation coefficients ($R^2 < 0.75$) which suggested a less significant role of multilayer adsorption and a weaker fit for heterogeneous surface behavior. Overall, the developed membrane overcame the permeability–selectivity trade-off as well as achieving high dye removal, antifouling, and adsorption for sustainable wastewater treatment. The variation in GR loadings across different formulations led to distinct morphological and functional characteristics which led to varied membrane performances. This highlights the critical role of nanofiller composition in tailoring membrane performance for specific separation and water treatment objectives.

Conflicts of interest

Authors decalare no conflicts of interest.

Data availability

Data described in this research is available on request.

Acknowledgements

Authors are acknowledging to Universiti Malaysia Sarawak for financial support grant no. UNI/F02/VC-HIRG/85516/P12-01/2022. This research is also funded by Princess Nourah bint Abdulrahman University Researchers Supporting Project number (PNURSP2025R80), Princess Nourah bint Abdulrahman University, Riyadh, Saudi Arabia.

References

1 R. Al-Tohamy, *et al.*, A critical review on the treatment of dye-containing wastewater: Ecotoxicological and health concerns of textile dyes and possible remediation approaches for environmental safety, *Ecotoxicol. Environ. Saf.*, 2022, **231**, 113160, DOI: **10.1016/j.ecoenv.2021.113160**.

2 P. O. Oladoye, T. O. Ajiboye, E. O. Omotola and O. J. Oyewola, Methylene blue dye: Toxicity and potential elimination technology from wastewater, *Results Eng.*, 2022, **16**, 100678, DOI: **10.1016/j.rineng.2022.100678**.

3 J. Fito, *et al.*, Adsorption of methylene blue from textile industrial wastewater using activated carbon developed from Rumex abyssinicus plant, *Sci. Rep.*, 2023, **13**(1), 5427, DOI: **10.1038/s41598-023-32341-w**.

4 B. A. Patel and C. S. Pereira, Process intensification at scale: An industrial perspective, *Chem. Eng. Process.*, 2022, **181**, 109098, DOI: **10.1016/j.cep.2022.109098**.

5 P. Loganathan, J. Kandasamy, H. Ratnaweera and S. Vigneswaran, Treatment Trends and Hybrid Methods for the Removal of Poly- and Perfluoroalkyl Substances from Water—A Review, *Appl. Sci.*, 2024, **14**(6), 2574, DOI: **10.3390/app14062574**.

6 A. T. Nguyen and L. Le Tran, A Review About the Occurrence and Effectiveness of Conventional and Advanced Treatment Technologies of Persistent Organic Pollutants in Surface Water, *Rev. Environ. Contam. Toxicol.*, 2024, **262**(1), 11, DOI: **10.1007/s44169-024-00062-4**.

7 N. Abdul Rahman, *et al.*, Kinetic modelling of peat water treatment with continuous electrocoagulation using aluminium electrodes, *J. Environ. Chem. Eng.*, 2023, **11**(3), 109559, DOI: **10.1016/j.jece.2023.109559**.

8 A. I. Osman, *et al.*, Membrane Technology for Energy Saving: Principles, Techniques, Applications, Challenges, and Prospects, *Adv. Energy Sustainability Res.*, 2024, **5**(5), 2400011, DOI: **10.1002/aesr.202400011**.

9 N. Abdul Rahman, *et al.*, Statistical analysis of salinity reduction in Borneo tropical brackish peat water with continuous electrocoagulation treatment system, *J. Hazard. Mater. Adv.*, 2023, **10**, 100265, DOI: **10.1016/j.hazadv.2023.100265**.

10 N. Abdul Rahman, *et al.*, Corrosion Resistance and Electrochemical Adaptation of Aluminium in Brackish Peat Water Sources Under Seawater Intrusion in the Rural Tropical Peatlands of Borneo, *Sustain. Chem. Clim. Action*, 2025, **6**, 100074, DOI: **10.1016/j.scca.2025.100074**.

11 C. Thamaraiselvan and R. Wickramasinghe, Recent progress on sustainable membrane manufacturing with green solvents and biopolymers, *Curr. Opin. Chem. Eng.*, 2025, **47**, 101092, DOI: **10.1016/j.coche.2025.101092**.

12 M. Q. Seah, S. F. Chua, W. L. Ang, W. J. Lau, A. Mansourizadeh and C. Thamaraiselvan, Advancements in polymeric membranes for challenging water filtration environments: A comprehensive review, *J. Environ. Chem. Eng.*, 2024, **12**(3), 112628, DOI: **10.1016/j.jece.2024.112628**.

13 D. S. Rajendran, *et al.*, Recent advances in various cleaning strategies to control membrane fouling: a comprehensive review, *Clean Technol. Environ. Policy*, 2025, **27**(2), 649–664, DOI: **10.1007/s10098-024-03000-z**.

14 A. James, *et al.*, Lithium Chloride-Mediated enhancement of dye removal capacity in Borneo bamboo derived nanocellulose-based nanocomposite membranes (NCMs), *J. Mol. Liq.*, 2024, **413**, 125973, DOI: **10.1016/j.molliq.2024.125973**.

15 A. James, *et al.*, A review of nanocellulose modification and compatibility barrier for various applications, *J. Thermoplast. Compos. Mater.*, 2023, **37**(6), 2149–2199, DOI: **10.1177/08927057231205451**.

16 Z. Chen, J. Xue, J. Zhang, J. Qu, K. Huang and M. Wang, Co-doped Zr-UiO-66-NH2@carboxylated cellulose nanocrystals/PAN membrane for oil/water separation with photocatalysis-PMS synergistic self-cleaning and antibacterial activity, *Int. J. Biol. Macromol.*, 2024, **282**, 137158, DOI: **10.1016/j.ijbiomac.2024.137158**.

17 Q. Fan, Z. Li, M. Li, X. Zhou, G. Zhang and S. Shen, In-situ generation of anti-fouling TpPa/PVDF membranes showing excellent photocatalytic degradation and self-cleaning for dyes in water, *Sep. Purif. Technol.*, 2024, **343**, 127167, DOI: **10.1016/j.seppur.2024.127167**.

18 N. I. Ibrahim, *et al.*, Characterization and isolation method of Gigantochloa scortechinii (Buluh Semantan) cellulose nanocrystals, *Int. J. Biol. Macromol.*, 2024, **272**, 132847, DOI: **10.1016/j.ijbiomac.2024.132847**.

19 Y. Jiang, *et al.*, Superoleophobic TiO2@SSM membranes with antifouling and photocatalytic ability for efficient microbubbles flotation emulsion separation and organic pollutants degradation, *J. Membr. Sci.*, 2024, **690**, 122217, DOI: **10.1016/j.memsci.2023.122217**.

20 M. Y. Akram, T. Ashraf, L. Tong, X. Yin, H. Dong and H. Lu, Architecting high-performance photocatalysts: A review of modified 2D/2D graphene/g-C3N4 heterostructures, *J. Environ. Chem. Eng.*, 2024, **12**(5), 113415, DOI: **10.1016/j.jece.2024.113415**.

21 J. Anthonette, *et al.*, A review of nanocellulose modification and compatibility barrier for various applications, *J. Thermoplast. Compos. Mater.*, 2023, **37**(6), 2149–2199, DOI: **10.1177/08927057231205451**.

22 M. Oprea, *et al.*, Improved Biomineralization Using Cellulose Acetate/Magnetic Nanoparticles Composite Membranes, *Polymers*, 2025, **17**(2), 209, DOI: **10.3390/polym17020209**.

23 X. Xu, *et al.*, Bioinspired multi-functional modified PVDF membrane for efficient oil-water separation, *Sep. Purif. Technol.*, 2025, **358**, 130410, DOI: **10.1016/j.seppur.2024.130410**.

24 Z. W. Heng, W. C. Chong, Y. L. Pang, L. C. Sim and C. H. Koo, Novel visible-light responsive NCQDs-TiO2/PAA/PES photocatalytic membrane with enhanced antifouling properties and self-cleaning performance, *J. Environ. Chem. Eng.*, 2021, **9**(4), 105388, DOI: **10.1016/j.jece.2021.105388**.

25 C. Zarzzeka, J. Goldoni, J. do R. de Paula de Oliveira, G. G. Lenzi, M. D. Bagatini and L. M. S. Colpini, Photocatalytic action of Ag/TiO2 nanoparticles to emerging pollutants degradation: a comprehensive review, *Sustain. Chem. Environ.*, 2024, **8**, 100177, DOI: **10.1016/j.scenv.2024.100177**.

26 K.-Y. Chan, C.-L. Li, D.-M. Wang and J.-Y. Lai, Formation of porous structures and crystalline phases in poly(vinylidene fluoride) membranes prepared with nonsolvent-induced phase separation- roles of solvent polarity, *Polymers*, 2023, **15**(5), 1314, DOI: **10.3390/polym15051314**.

27 J. E. Marshall, *et al.*, On the solubility and stability of polyvinylidene fluoride, *Polymers*, 2021, **13**(9), 1354, DOI: **10.3390/polym13091354**.

28 A. Z. Sueraya, *et al.*, Impact of titanium dioxide/graphene in polyvinylidene fluoride nanocomposite membrane to intensify methylene blue dye removal, antifouling performance, and reusability, *J. Appl. Polym. Sci.*, 2024, **141**(47), e57648, DOI: **10.1002/app.56257**.

29 M. R. Rahman, *et al.*, A TiO2 grafted bamboo derivative nanocellulose polyvinylidene fluoride (PVDF) nanocomposite membrane for wastewater treatment by a photocatalytic process, *Mater. Adv.*, 2024, **5**(19), 7617–7636, DOI: **10.1039/D4MA00716F**.

30 R. Mohamat, *et al.*, Incorporation of different polymeric additives for polyvinylidene fluoride membrane fabrication and its performance on methylene blue rejection and antifouling improvement, *J. Polym. Environ.*, 2023, **31**(8), 3466–3479, DOI: **10.1007/s10924-023-02774-5**.

31 A. James, *et al.*, Lithium Chloride-Mediated enhancement of dye removal capacity in Borneo bamboo derived nanocellulose-based nanocomposite membranes (NCMs), *J. Mol. Liq.*, 2024, **413**, 125973, DOI: **10.1016/j.molliq.2024.125973**.

32 ASTM E168-16, "*Standard Practices for General Techniques of Infrared Quantitative Analysis*", ASTM International, West Conshohocken, PA, USA.

33 ASTM E1252-98, "*Standard Practice for General Techniques for Obtaining Infrared Spectra for Qualitative Analysis*", ASTM International, West Conshohocken, PA, USA.

34 ASTM F3419-22, "*Standard Test Method for Mineral Characterization of Equine Surface Materials by X-Ray Diffraction (XRD) Techniques*", ASTM International, West Conshohocken, PA, USA.

35 ASTM E3-11, "*Standard Guide for Preparation of Metallographic Specimens*", ASTM International, West Conshohocken, PA, US.

36 P. Boruah, R. Gupta and V. Katiyar, Fabrication of cellulose nanocrystal (CNC) from waste paper for developing antifouling and high-performance polyvinylidene fluoride (PVDF) membrane for water purification, *Carbohydr. Polym. Technol. Appl.*, 2023, **5**, 100309, DOI: **10.1016/j.carpta.2023.100309**.

37 A. Omar, *et al.*, Investigation of morphological, structural and electronic transformation of PVDF and ZnO/rGO/PVDF hybrid membranes, *Opt. Quantum Electron.*, 2023, **55**(4), 381, DOI: **10.1007/s11082-023-04663-6**.

38 ASTM E169-16, "*Standard Practices for General Techniques of Ultraviolet-Visible Quantitative Analysis*", ASTM International, West Conshohocken, PA, USA.

39 L. Ruan, X. Yao, Y. Chang, L. Zhou, G. Qin and X. Zhang, Properties and applications of the β phase Poly(vinylidene fluoride), *Polymers*, 2018, **10**(3), 228, DOI: **10.3390/polym10030228**.

40 R. Sivaranjanee, P. S. Kumar and S. Mahalaxmi, A review on agro-based materials on the separation of environmental pollutants from water system, *Chem. Eng. Res. Des.*, 2022, **181**, 423–457, DOI: **10.1016/j.cherd.2022.04.002**.

41 X. Chen, Y. Ren, G. Qu, Z. Wang, Y. Yang and P. Ning, A review of environmental functional materials for cyanide removal by adsorption and catalysis, *Inorg. Chem. Commun.*, 2023, **157**, 111298, DOI: **10.1016/j.inoche.2023.111298**.

42 A. Jahangir, U. A. K. M. Atique and U. Mohammad Nasir, Isotherm and kinetic modeling of Cd(II) uptake from aqueous solutions using an agri-waste bisorbent jute stick

powder, *Braz. J. Anal. Chem.*, 2020, 7(28), 31–43, DOI: 10.30744/brjac.2179-3425.AR-20-2020.

43 J. Wang and X. Guo, Adsorption kinetic models: physical meanings, applications, and solving methods, *J. Hazard. Mater.*, 2020, **390**, 122156, DOI: 10.1016/j.jhazmat.2020.122156.

44 N. Abdul Rahman, *et al.*, Treatment of tropical peat water in Sarawak peatlands nature reserve by utilising a batch electrocoagulation system, *Sustain. Chem. Environ.*, 2023, **4**, 100043, DOI: 10.1016/j.scenv.2023.100043.

45 P. Kaspar, *et al.*, Characterization of polyvinylidene fluoride (PVDF) electrospun fibers doped by carbon flakes, *Polymers*, 2020, **12**(12), 2766, DOI: 10.3390/polym12122766.

46 D. D. Chronopoulos, A. Bakandritsos, M. Pykal, R. Zbořil and M. Otyepka, Chemistry, properties, and applications of fluorographene, *Appl. Mater. Today*, 2017, **9**, 60–70, DOI: 10.1016/j.apmt.2017.05.004.

47 E. Gontarek-Castro, M. K. Rybarczyk, R. Castro-Muñoz, M. Morales-Jiménez, B. Barragán-Huerta and M. Lieder, Characterization of PVDF/graphene nanocomposite membranes for water desalination with enhanced antifungal activity, *Water*, 2021, **13**(9), 1279, DOI: 10.3390/w13091279.

48 C. Athanasekou, *et al.*, Mixed matrix PVDF/graphene and composite-skin PVDF/graphene oxide membranes applied in membrane distillation, *Polym. Eng. Sci.*, 2019, **59**(S1), E262–E278, DOI: 10.1002/pen.24930.

49 X. Han, *et al.*, Effect of π–π stacking interfacial interaction on the properties of graphene/poly(styrene-b-isoprene-b-styrene) composites, *Nanomaterials*, 2021, **11**(9), 2158, DOI: 10.3390/nano11092158.

50 J. Zhan, Z. Lei and Y. Zhang, Non-covalent interactions of graphene surface: mechanisms and applications, *Chem*, 2022, **8**(4), 947–979, DOI: 10.1016/j.chempr.2021.12.015.

51 Z. Guo, *et al.*, Surface functionalization of graphene-based materials: biological behavior, toxicology and safe-by-design aspects, *Adv. Biol.*, 2021, **5**(9), 2100637, DOI: 10.1002/adbi.202100637.

52 W. Iken, *et al.*, Effects of van der Waals interactions on the dipole moment and adsorption energy of H2O on Au(100) and Cu(100) surfaces: density functional theory study, *J. Indian Chem. Soc.*, 2025, **102**(2), 101597, DOI: 10.1016/j.jics.2025.101597.

53 W. K. Wan Ramli, N. Dollah and O. L. Qing, TiO2/polysulfone composite membrane for enhanced removal of acetaminophen from water, *J. Phys. Sci.*, 2024, **35**(3), 1–15, DOI: 10.21315/jps2024.35.3.1.

54 J.-W. Lee, S.-P. Jeong, N.-H. You and S.-Y. Moon, Tunable synthesis of predominant semi-ionic and covalent fluorine bonding states on a graphene surface, *Nanomaterials*, 2021, **11**(4), 942, DOI: 10.3390/nano11040942.

55 D. Prodan, *et al.*, Synthesis and characterization of some graphene oxide powders used as additives in hydraulic mortars, *Appl. Sci.*, 2021, **11**(23), 11330, DOI: 10.3390/app112311330.

56 N. Yahya, A. M. Ali, F. A. Wahaab and S. Sikiru, Spectroscopic analysis of the adsorption of carbon based nanoparticles on reservoir sandstones, *J. Mater. Res. Technol.*, 2020, **9**(3), 4326–4339, DOI: 10.1016/j.jmrt.2020.02.058.

57 A. Abdel-Karim, *et al.*, PVDF membranes containing reduced graphene oxide: effect of degree of reduction on membrane distillation performance, *Desalination*, 2019, **452**, 196–207, DOI: 10.1016/j.desal.2018.11.014.

58 A. A. B. Omran, *et al.*, Micro- and nanocellulose in polymer composite materials: a review, *Polymers*, 2021, **13**(2), 231, DOI: 10.3390/polym13020231.

59 S. S. Shazleen, T. A. T. Yasim-Anuar, N. A. Ibrahim, M. A. Hassan and H. Ariffin, Functionality of cellulose nanofiber as bio-based nucleating agent and nano-reinforcement material to enhance crystallization and mechanical properties of polylactic acid nanocomposite, *Polymers*, 2021, **13**(3), 389, DOI: 10.3390/polym13030389.

60 C. Shuai, *et al.*, Cellulose nanocrystals as biobased nucleation agents in poly-l-lactide scaffold: Crystallization behavior and mechanical properties, *Polym. Test.*, 2020, **85**, 106458, DOI: 10.1016/j.polymertesting.2020.106458.

61 A. Etale, A. J. Onyianta, S. R. Turner and S. J. Eichhorn, Cellulose: a review of water interactions, applications in composites and water treatment, *Chem. Rev.*, 2023, **123**(5), 2016–2048, DOI: 10.1021/acs.chemrev.2c00477.

62 N. Ismail, M. Essalhi, M. Rahmati, Z. Cui, M. Khayet and N. Tavajohi, Experimental and theoretical studies on the formation of pure β-phase polymorphs during fabrication of polyvinylidene fluoride membranes by cyclic carbonate solvents, *Green Chem.*, 2021, **23**(5), 2130–2147, DOI: 10.1039/D1GC00122A.

63 S. Acarer-Arat, M. Tüfekci, İ. Pir and N. Tüfekci, Nanocellulose in polyvinylidene fluoride (PVDF) membranes: assessing reinforcement impact and modelling techniques, *J. Environ. Chem. Eng.*, 2024, **12**(6), 114749, DOI: 10.1016/j.jece.2024.114749.

64 W. Zhang, *et al.*, The preparation, structural design and application of electroactive poly (vinylidene fluoride) -based materials for wearable sensors and human energy harvesters, *Polymers*, 2023, **15**(13), 2766, DOI: 10.3390/polym15132766.

65 E. Gontarek-Castro, G. Di Luca, M. Lieder and A. Gugliuzza, Graphene-coated PVDF membranes: effects of multi-scale rough structure on membrane distillation performance, *Membranes*, 2022, **12**(5), 511, DOI: 10.3390/membranes12050511.

66 L.-T. Lee and Y.-L. Ke, Superior crystallization kinetics caused by the remarkable nucleation effect of graphene oxide in novel ternary biodegradable polymer composites, *ACS Omega*, 2020, **5**(47), 30643–30656, DOI: 10.1021/acsomega.0c04658.

67 M. A. Chowdhury, *et al.*, Novel energy bandgap formation of organic solution doped graphene membrane for semiconductor applications, *Appl. Surf. Sci. Adv.*, 2023, **13**, 100373, DOI: 10.1016/j.apsadv.2023.100373.

68 A. Alkhouzaam and H. Qiblawey, Functional GO-based membranes for water treatment and desalination: Fabrication methods, performance and advantages. A review, *Chemosphere*, 2021, **274**, 129853, DOI: **10.1016/j.chemosphere.2021.129853**.

69 Y. R. Taha, *et al.*, Optimum content of incorporated nanomaterials: Characterizations and performance of mixed matrix membranes a review, *Desalin. Water Treat.*, 2024, **317**, 100088, DOI: **10.1016/j.dwt.2024.100088**.

70 C. Jeong, F. W. Starr, K. L. Beers and J. F. Douglas, Influence of functionalization on the crystallinity and basic thermodynamic properties of polyethylene, *Macromolecules*, 2023, **56**(11), 3873–3883, DOI: **10.1021/acs.macromol.2c02569**.

71 S. Alexander and M. Alidu, *Recovery of Cellulose from Food and Agricultural Waste*, 2025, DOI: **10.5772/intechopen.1009308**.

72 S. S. Panicker, S. P. Rajeev and V. Thomas, Harnessing multi-effect energy harvesting: triboelectric, piezoelectric, and flexoelectric synergies of hBN in PDMS nanogenerators for high-performance wearable devices, *J. Mater. Sci.*, 2025, **60**(23), 9698–9720, DOI: **10.1007/s10853-025-11004-3**.

73 W. Kh. Al-Musawy, B. M. Ibraheem, T. M. Darwesh, M. H. Al-Furaiji, M. Awad and Q. F. Alsalhy, Synthesis and performance of polysulfone-chitosan ultrafiltration membranes for humic acid removal, *Desalin. Water Treat.*, 2025, **321**, 100939, DOI: **10.1016/j.dwt.2024.100939**.

74 J. Chae, T. Lim, H. Cheng, J. Hu, S. Kim and W. Jung, Graphene oxide and carbon nanotubes-based polyvinylidene fluoride membrane for highly increased water treatment, *Nanomaterials*, 2021, **11**(10), 2498, DOI: **10.3390/nano11102498**.

75 H. Jahandideh, J.-R. Macairan, A. Bahmani, M. Lapointe and N. Tufenkji, Fabrication of graphene-based porous materials: traditional and emerging approaches, *Chem. Sci.*, 2022, **13**(31), 8924–8941, DOI: **10.1039/D2SC01786E**.

76 B. Arundhathi, M. Pabba, S. S. Raj, N. Sahu and S. Sridhar, Advancements in mixed-matrix membranes for various separation applications: state of the art and future prospects, *Membranes*, 2024, **14**(11), 224, DOI: **10.3390/membranes14110224**.

77 H. Roberge, P. Moreau, E. Couallier and P. Abellan, Determination of the key structural factors affecting permeability and selectivity of PAN and PES polymeric filtration membranes using 3D FIB/SEM, *J. Membr. Sci.*, 2022, **653**, 120530, DOI: **10.1016/j.memsci.2022.120530**.

78 K. H. Leopold, *et al.*, Design of sponge-like PES hollow fiber membranes using the environmentally friendly solvent N,N-dimethyl lactamide, *Sep. Purif. Technol.*, 2025, **365**, 132625, DOI: **10.1016/j.seppur.2025.132625**.

79 S. T. Ghaly, U. N. Eldemerdash and A. H. El-Shazly, Morphology and thermodynamic study of a novel composite membrane from waste polystyrene/slag: experimental investigation, *ACS Omega*, 2024, **9**(22), 23512–23522, DOI: **10.1021/acsomega.4c00671**.

80 S. Alyarnezhad, *et al.*, Polyvinylidene fluoride-graphene oxide membranes for dye removal under visible light irradiation, *Polymers*, 2020, **12**(7), 1509, DOI: **10.3390/polym12071509**.

81 S. Kluge, T. Kose and M. Tutuş, Tuning the morphology and gas separation properties of polysulfone membranes, *Membranes*, 2022, **12**(7), 654, DOI: **10.3390/membranes12070654**.

82 L. Tjale, H. Richards, O. Mahlangu and L. N. Nthunya, Silica nanoparticle modified polysulfone/polypropylene membrane for separation of oil-water emulsions, *Results Eng.*, 2022, **16**, 100623, DOI: **10.1016/j.rineng.2022.100623**.

83 S. Mohsenpour, S. Leaper, J. Shokri, M. Alberto and P. Gorgojo, Effect of graphene oxide in the formation of polymeric asymmetric membranes *via* phase inversion, *J. Membr. Sci.*, 2022, **641**, 119924, DOI: **10.1016/j.memsci.2021.119924**.

84 R. Mohamat, *et al.*, Incorporation of different polymeric additives for polyvinylidene fluoride membrane fabrication and its performance on methylene blue rejection and antifouling improvement, *J. Polym. Environ.*, 2023, **31**(8), 3466–3479, DOI: **10.1007/s10924-023-02774-5**.

85 S. O. Ilyin, *et al.*, The effect of non-solvent nature on the rheological properties of cellulose solution in diluted ionic liquid and performance of nanofiltration membranes, *Int. J. Mol. Sci.*, 2023, **24**(9), 8057, DOI: **10.3390/ijms24098057**.

86 A. E. Mahdi, *et al.*, Preparation, characterization and applications of polyethersulfone/bentonite clay composite for protein removal, *Desalin. Water Treat.*, 2024, **320**, 100653, DOI: **10.1016/j.dwt.2024.100653**.

87 P. Tshindane, B. B. Mamba, M. M. Motsa and T. T. I. Nkambule, Delayed solvent-nonsolvent demixing preparation and performance of a highly permeable polyethersulfone ultrafiltration membrane, *Membranes*, 2022, **13**(1), 39, DOI: **10.3390/membranes13010039**.

88 X. Dong, D. Lu, T. A. L. Harris and I. C. Escobar, Polymers and solvents used in membrane fabrication: a review focusing on sustainable membrane development, *Membranes*, 2021, **11**(5), 309, DOI: **10.3390/membranes11050309**.

89 S. Dhameri, *et al.*, Impact of additives on poly (acrylonitrile-butadiene-styrene) membrane formulation process using non-solvent-induced phase separation, *Membranes*, 2025, **15**(6), 181, DOI: **10.3390/membranes15060181**.

90 M. S. A. Hamzah, *et al.*, Preparation of the electrospun polyvinylidene fluoride/polyvinyl alcohol scaffold as a potential tissue replacement, *IIUM Eng J.*, 2021, **22**(1), 245–258, DOI: **10.31436/iiumej.v22i1.1548**.

91 J. Sharma, C. Totee, V. Kulshrestha and B. Ameduri, Spectroscopic evidence and mechanistic insights on dehydrofluorination of PVDF in alkaline medium, *Eur. Polym. J.*, 2023, **201**, 112580, DOI: **10.1016/j.eurpolymj.2023.112580**.

92 V. O. C. Concha, *et al.*, Properties, characterization and biomedical applications of polyvinylidene fluoride (PVDF):

a review, *J. Mater. Sci.*, 2024, **59**(31), 14185–14204, DOI: 10.1007/s10853-024-10046-3.

93 I. Sriyanti, *et al.*, Physicochemical and mechanical properties of polyvinylidene fluoride nanofiber membranes, *Case Stud. Chem. Environ. Eng.*, 2024, **9**, 100588, DOI: 10.1016/j.cscee.2023.100588.

94 L. Chen, P. Xu and H. Wang, Interplay of the factors affecting water flux and salf rejection in membrane distillation: a state-of-the-art critical review, *Water*, 2020, **12**(10), 2841, DOI: 10.3390/w12102841.

95 F. Fallahianbijan, S. Giglia, C. Carbrello and A. L. Zydney, Quantitative analysis of internal flow distribution and pore interconnectivity within asymmetric virus filtration membranes, *J. Membr. Sci.*, 2020, **595**, 117578, DOI: 10.1016/j.memsci.2019.117578.

96 F. Tibi, S.-J. Park and J. Kim, Improvement of membrane distillation using PVDF membrane incorporated with TiO2 modified by silane and optimization of fabricating conditions, *Membranes*, 2021, **11**(2), 95, DOI: 10.3390/membranes11020095.

97 L. A. Belyaeva, C. Tang, L. Juurlink and G. F. Schneider, Macroscopic and microscopic wettability of graphene, *Langmuir*, 2021, **37**(14), 4049–4055, DOI: 10.1021/acs.langmuir.0c02817.

98 M. A. Ahmed, S. Amin and A. A. Mohamed, Fouling in reverse osmosis membranes: monitoring, characterization, mitigation strategies and future directions, *Heliyon*, 2023, **9**(4), e14908, DOI: 10.1016/j.heliyon.2023.e14908.

99 D. Kim, *et al.*, Wettability of graphene and interfacial water structure, *Chem*, 2021, **7**(6), 1602–1614, DOI: 10.1016/j.chempr.2021.03.006.

100 C. Soto, *et al.*, Free volume and permeability of mixed matrix membranes made from a Terbutil-M-terphenyl Polyamide and a porous polymer network, *Polymers*, 2022, **14**(15), 3176, DOI: 10.3390/polym14153176.

101 T. Kusworo, R. E. Nugraheni and N. Aryanti, The effect of membrane modification using TiO2, ZnO, and GO nanoparticles: challenges and future direction in wastewater treatment, *IOP Conf. Ser.:Mater. Sci. Eng.*, 2021, **1053**(1), 012135, DOI: 10.1088/1757-899X/1053/1/012135.

102 A. M. Sofyana, M. D. Supardan, A. C. Ambarita and N. Arahman, Combination of cellulose nanocrystal and graphene oxide as modifying agent for improving the performance of PVDF membranes, *Case Stud. Chem. Environ. Eng.*, 2024, **10**, 100873, DOI: 10.1016/j.cscee.2024.100873.

103 A. M. Shawky, Y. H. Kotp, M. A. Mousa, M. M. S. Aboelfadl, E. E. Hekal and K. Zakaria, Effect of titanium oxide/reduced graphene (TiO2/rGO) addition onto water flux and reverse salt diffusion thin-film nanocomposite forward osmosis membranes, *Environ. Sci. Pollut. Res.*, 2024, **31**(16), 24584–24598, DOI: 10.1007/s11356-024-32500-0.

104 N. Katagiri, T. Uchida, H. Takahashi and E. Iritani, An evaluation of the relationship between membrane properties and the fouling mechanism based on a blocking filtration model, *Separations*, 2024, **11**(3), 70, DOI: 10.3390/separations11030070.

105 M. Khansanami and A. Esfandiar, High flux and complete dyes removal from water by reduced graphene oxide laminate on Poly Vinylidene Fluoride/graphene oxide membranes, *Environ. Res.*, 2021, **201**, 111576, DOI: 10.1016/j.envres.2021.111576.

106 M. Edokali, *et al.*, Antifouling and stability enhancement of electrochemically modified reduced graphene oxide membranes for water desalination by forward osmosis, *J. Water Proc. Eng.*, 2024, **59**, 104809, DOI: 10.1016/j.jwpe.2024.104809.

107 T. Zhao, F. Wang, X. Hu and D. Kong, A novel graphene oxide electrode preparation and its performance in the treatment of saline organic wastewater, *Desalin. Water Treat.*, 2024, **318**, 100316, DOI: 10.1016/j.dwt.2024.100316.

108 R. Mohamat, *et al.*, Methylene blue rejection and antifouling properties of different carbonaceous additives-based polyvinylidene fluoride membrane, *Mater. Today Commun.*, 2023, **35**, 105862, DOI: 10.1016/j.mtcomm.2023.105862.

109 R. Mohamat, *et al.*, Incorporation of graphene oxide/titanium dioxide with different polymer materials and its effects on methylene blue dye rejection and antifouling ability, *Environ. Sci. Pollut. Res.*, 2023, **30**(28), 72446–72462, DOI: 10.1007/s11356-023-27207-7.

110 A. M. Lima, A. M. de Oliveira, T. G. de Sousa, A. C. Pereira, R. B. de Carvalho and W. A. Pinheiro, Filtration membranes of reduced graphene oxide for dye removal – production and characterization, *Desalin. Water Treat.*, 2022, **278**, 217–225, DOI: 10.5004/dwt.2022.29027.

111 T. Zhang, *et al.*, Integrated dual antifouling mechanism onto graphene oxide membranes for dye wastewater treatment: Synergistic effects of photocatalytic and antimicrobial, *Sep. Purif. Technol.*, 2025, 134356, DOI: 10.1016/j.seppur.2025.134356.

112 J. M. Luque-Alled, *et al.*, Polyethersulfone membranes: from ultrafiltration to nanofiltration *via* the incorporation of APTS functionalized-graphene oxide, *Sep. Purif. Technol.*, 2020, **230**, 115836, DOI: 10.1016/j.seppur.2019.115836.

113 T. A. Otitoju, M. Ahmadipour, S. Li, N. F. Shoparwe, L. X. Jie and A. L. Owolabi, Influence of nanoparticle type on the performance of nanocomposite membranes for wastewater treatment, *J. Water Proc. Eng.*, 2020, **36**, 101356, DOI: 10.1016/j.jwpe.2020.101356.

114 N. Mehrabi, H. Lin and N. Aich, Deep eutectic solvent functionalized graphene oxide nanofiltration membranes with superior water permeance and dye desalination performance, *Chem. Eng. J.*, 2021, **412**, 128577, DOI: 10.1016/j.cej.2021.128577.

115 R. J. Kadhim, F. H. Al-Ani, M. Al-shaeli, Q. F. Alsalhy and A. Figoli, Removal of dyes using graphene oxide (GO) mixed matrix membranes, *Membranes*, 2020, **10**(12), 366, DOI: 10.3390/membranes10120366.

116 X. Wang, *et al.*, Graphene oxide membranes using MOF@Chitosan core-shell nanoparticles as dual

modulators for dye separation, *Chem. Synth.*, 2024, **4**(2), DOI: **10.20517/cs.2023.60**.

117 X. Sun, *et al.*, Enhancing the performance of PVDF/GO ultrafiltration membrane *via* improving the dispersion of GO with homogeniser, *Membranes*, 2022, **12**(12), 1268, DOI: **10.3390/membranes12121268**.

118 N. T. Ndeh, S. Sairiam and R. Nuisin, Graphene oxide-chitosan coated PVDF adsorptive microfiltration membrane: Enhancing dye removal and antifouling properties, *Int. J. Biol. Macromol.*, 2024, **282**, 137005, DOI: **10.1016/j.ijbiomac.2024.137005**.

119 J. O. Eniola, *et al.*, Advances in electrochemical membranes for water treatment: a comprehensive review, *Desalin. Water Treat.*, 2024, **319**, 100450, DOI: **10.1016/j.dwt.2024.100450**.

120 D. R. Rout, H. M. Jena, O. Baigenzhenov and A. Hosseini-Bandegharaei, Graphene-based materials for effective adsorption of organic and inorganic pollutants: a critical and comprehensive review, *Sci. Total Environ.*, 2023, **863**, 160871, DOI: **10.1016/j.scitotenv.2022.160871**.

121 B. Bhushan, P. Negi, A. Nayak and S. Goyal, Graphene composites for water remediation: an overview of their advanced performance with focus on challenges and future prospects, *Adv. Compos. Hybrid Mater.*, 2025, **8**(1), 55, DOI: **10.1007/s42114-024-01088-x**.

122 J. Wang, S. C. Abbas, L. Li, C. C. Walker, Y. Ni and Z. Cai, Cellulose membranes: synthesis and applications for water and gas separation and purification, *Membranes*, 2024, **14**(7), 148, DOI: **10.3390/membranes14070148**.

123 H. Zhang, Y. Zheng, S. Yu, W. Chen and J. Yang, A review of advancing two-dimensional material membranes for ultrafast and highly selective liquid separation, *Nanomaterials*, 2022, **12**(12), 2103, DOI: **10.3390/nano12122103**.

124 M. G. Shin, J. Y. Seo, H. Park, Y.-I. Park and J.-H. Lee, Overcoming the permeability-selectivity trade-off of desalination membranes *via* controlled solvent activation, *J. Membr. Sci.*, 2021, **620**, 118870, DOI: **10.1016/j.memsci.2020.118870**.

125 Y. Ibrahim, M. Khatri, N. K. Khanzada and N. Hilal, Electrically conductive membranes featuring integrated porous feed spacers for superior antifouling performance, *npj Clean Water*, 2025, **8**(1), 64, DOI: **10.1038/s41545-025-00497-9**.

126 V. O. Ng, X. Hong, H. Yu, H. Wu and Y. M. Hung, Anomalously enhanced thermal performance of micro heat pipes coated with heterogeneous superwettable graphene nanostructures, *Appl. Energy*, 2022, **326**, 119994, DOI: **10.1016/j.apenergy.2022.119994**.

127 Y. Mao, *et al.*, Hydrophobic metal-organic framework@graphene oxide membrane with enhanced water transport for desalination, *J. Membr. Sci.*, 2023, **669**, 121324, DOI: **10.1016/j.memsci.2022.121324**.

128 H. Deng, J. Huang, C. Qin, T. Xu, H. Ni and P. Ye, Preparation of high-performance nanocomposite membranes with hydroxylated graphene and graphene oxide, *J. Water Proc. Eng.*, 2021, **40**, 101945, DOI: **10.1016/j.jwpe.2021.101945**.

129 A. R. Marlinda, *et al.*, Tailoring hydrophobicity properties of polyvinylidene fluoride infused graphene composite films, *Mater. Sci.-Pol.*, 2022, **40**(3), 72–79, DOI: **10.2478/msp-2022-0032**.

130 M. Yang, *et al.*, Simple fabrication of polyvinylidene fluoride/graphene composite membrane with good lipophilicity for oil treatment, *ACS Omega*, 2022, **7**(25), 21454–21464, DOI: **10.1021/acsomega.2c00764**.

131 S. K. Tiwary, M. Singh, S. V. Chavan and A. Karim, Graphene oxide-based membranes for water desalination and purification, *npj 2D Mater. Appl.*, 2024, **8**(1), 27, DOI: **10.1038/s41699-024-00462-z**.

132 H. M. Mousa, H. S. Fahmy, G. A. M. Ali, H. N. Abdelhamid and M. Ateia, Membranes for oil/water separation: a review, *Adv. Mater. Interfaces*, 2022, **9**(27), 2200557, DOI: **10.1002/admi.202200557**.

133 R. Zhang, C. Deng, X. Hou, T. Li, Y. Lu and F. Liu, Preparation and characterization of a Janus membrane with an 'integrated' structure and adjustable hydrophilic layer thickness, *Membranes*, 2023, **13**(4), 415, DOI: **10.3390/membranes13040415**.

134 A. Ghareeb, A. Fouda, R. M. Kishk and W. M. El Kazzaz, Unlocking the potential of titanium dioxide nanoparticles: an insight into green synthesis, optimizations, characterizations, and multifunctional applications, *Microb. Cell Fact.*, 2024, **23**(1), 341, DOI: **10.1186/s12934-024-02609-5**.

135 Y. Xu, S. L. Chiam, C. P. Leo and Z. Hu, Recent advances in photocatalytic TiO2-based membranes for eliminating water pollutants, *Sep. Purif. Rev.*, 2025, 1–18, DOI: **10.1080/15422119.2025.2487991**.

136 C. Zarzzeka, J. Goldoni, J. do R. de Paula de Oliveira, G. G. Lenzi, M. D. Bagatini and L. M. S. Colpini, Photocatalytic action of Ag/TiO2 nanoparticles to emerging pollutants degradation: a comprehensive review, *Sustain. Chem. Environ.*, 2024, **8**, 100177, DOI: **10.1016/j.scenv.2024.100177**.

137 A. Kutuzova, T. Dontsova and W. Kwapinski, Application of TiO2-based photocatalysts to antibiotics degradation: causes of sulfamethoxazole, trimethoprim and ciprofloxacin, *Catalysts*, 2021, **11**(6), 728, DOI: **10.3390/catal11060728**.

138 N. T. Padmanabhan, *et al.*, Graphene coupled TiO2 photocatalysts for environmental applications: a review, *Chemosphere*, 2021, **271**, 129506, DOI: **10.1016/j.chemosphere.2020.129506**.

139 M. Zubair, I.-H. Svenum, M. Rønning and J. Yang, Core-shell nanostructures of graphene-wrapped CdS nanoparticles and TiO2 (CdS@G@TiO2): the role of graphene in enhanced photocatalytic H2 generation, *Catalysts*, 2020, **10**(4), 358, DOI: **10.3390/catal10040358**.

140 S. A. Mousa, H. Abdallah, S. S. Ibrahim and S. A. Khairy, Enhanced photocatalytic properties of graphene oxide/polyvinylchloride membranes by incorporation with green prepared SnO2 and TiO2 nanocomposite for water treatment, *Appl. Phys. A:Mater. Sci. Process.*, 2023, **129**(12), 831, DOI: **10.1007/s00339-023-07117-8**.

141 A. Popa, M. Stefan, S. Macavei, I. Perhaita, L. B. Tudoran and D. Toloman, Facile preparation of PVDF/CoFe2O4-ZnO hybrid membranes for water depollution, *Polymers*, 2023, **15**(23), 4547, DOI: **10.3390/polym15234547**.

142 M. Namakka, M. R. Rahman, K. A. Mohamad Bin Said, M. Abdul Mannan and A. M. Patwary, A review of nanoparticle synthesis methods, classifications, applications, and characterization, *Environ. Nanotechnol., Monit. Manage.*, 2023, **20**(100900), 1532–2215, DOI: **10.1016/j.enmm.2023.100900**.

143 J. Zhang, *et al.*, Photocatalysis coupling with membrane technology for sustainable and continuous purification of wastewater, *Sep. Purif. Technol.*, 2024, **329**, 125225, DOI: **10.1016/j.seppur.2023.125225**.

144 L. Solhi, *et al.*, Understanding nanocellulose- water interactions: turning a detriment into an asset, *Chem. Rev.*, 2023, **123**(5), 1925–2015, DOI: **10.1021/acs.chemrev.2c00611**.

145 C. Yang, *et al.*, Research progress on improving dispersion stability of nanocellulose in different media: a review, *Int. J. Biol. Macromol.*, 2025, **304**, 140967, DOI: **10.1016/j.ijbiomac.2025.140967**.

146 A. Aguilar-Sanchez, *et al.*, Waterborne nanocellulose coatings for improving the antifouling and antibacterial properties of polyethersulfone membranes, *J. Membr. Sci.*, 2021, **620**, 118842, DOI: **10.1016/j.memsci.2020.118842**.

147 Y. Chen, *et al.*, Coral-inspired hierarchical vine-like structure surfaces: unveiling hydration layer synergistic effects for advanced antifouling membrane design, *J. Membr. Sci.*, 2025, **734**, 124472, DOI: **10.1016/j.memsci.2025.124472**.

148 N. N. R. Ahmad, A. W. Mohammad, E. Mahmoudi, W. L. Ang, C. P. Leo and Y. H. Teow, An overview of the modification strategies in developing antifouling nanofiltration membranes, *Membranes*, 2022, **12**(12), 1276, DOI: **10.3390/membranes12121276**.

149 N. F. Zulkefli, *et al.*, Recent mitigating strategies on membrane fouling for oily wastewater treatment, *Membranes*, 2021, **12**(1), 26, DOI: **10.3390/membranes12010026**.

150 Y. Ibrahim, V. Naddeo, F. Banat and S. W. Hasan, Preparation of novel polyvinylidene fluoride (PVDF)-Tin(IV) oxide (SnO2) ion exchange mixed matrix membranes for the removal of heavy metals from aqueous solutions, *Sep. Purif. Technol.*, 2020, **250**, 117250, DOI: **10.1016/j.seppur.2020.117250**.

151 Z. Cheng, H. Ye, F. Cheng, H. Li, Y. Ma, Q. Zhang, A. Natan, A. Mukhopadhyay, Y. Jiao, Y. Li, Y. Liu and H. Zhu, Tuning Chiral Nematic Pitch of Bioresourced Photonic Films via Coupling Organic Acid Hydrolysis, *Adv. Mater. Interfaces*, 2019, **6**(7), 1–12, DOI: **10.1002/admi.201802010**.

152 N. Hamri, *et al.*, Enhanced adsorption capacity of methylene blue dye onto kaolin through acid treatment: batch adsorption and machine learning studies, *Water*, 2024, **16**(2), 243, DOI: **10.3390/w16020243**.

153 J. Saleem, *et al.*, Adsorbent-embedded polymeric membranes for efficient dye-water treatment, *Polymers*, 2024, **16**(11), 1459, DOI: **10.3390/polym16111459**.

154 T. A. Saleh, Isotherm models of adsorption processes on adsorbents and nanoadsorbents, *Interface Sci. Technol.*, 2022, **34**, 99–126, DOI: **10.1016/B978-0-12-849876-7.00009-9**.

155 A. Waheed, N. Baig, N. Ullah and W. Falath, Removal of hazardous dyes, toxic metal ions and organic pollutants from wastewater by using porous hyper-cross-linked polymeric materials: a review of recent advances, *J. Environ. Manage.*, 2021, **287**, 112360, DOI: **10.1016/j.jenvman.2021.112360**.

156 R. Zangi, Breakdown of Langmuir Adsorption Isotherm in Small Closed Systems., *Langmuir*, 2024, **40**(7), 3900, DOI: **10.1021/acs.langmuir.3c03894**.

157 S. Mohammadpourfazeli, S. Arash, A. Ansari, S. Yang, K. Mallick and R. Bagherzadeh, Future prospects and recent developments of polyvinylidene fluoride (PVDF) piezoelectric polymer; fabrication methods, structure, and electro-mechanical properties, *RSC Adv.*, 2023, **13**(1), 370–387, DOI: **10.1039/D2RA06774A**.

158 C.-H. Kim, *et al.*, Controlling the polymorphs of PVDF membranes: Effects of a salt additive on PVDF polarization during phase separation processes, *Sep. Purif. Technol.*, 2024, **351**, 128120, DOI: **10.1016/j.seppur.2024.128120**.

159 T. D. Khue, *et al.*, Efficient adsorption of organic dyes using Fe3O4/carbon sphere nanocomposites: synthesis and performance evaluation, *J. Sci.:Adv. Mater. Devices*, 2025, **10**(2), 100880, DOI: **10.1016/j.jsamd.2025.100880**.

160 A. Sharma, S. Datta, R. K. Sanjana, B. M. Pooja, S. Bose and G. Hegde, Onion peel derived carbon nanoparticles incorporated polysulfone membranes: enhanced dye removal from water, *RSC Adv.*, 2025, **15**(10), 7786–7798, DOI: **10.1039/D5RA00025D**.

161 G. da C. Dias, *et al.*, PVDF/RGO membranes and the potential of adsorption technology: rhodamine dye removal, *Contrib. Cienc. Soc.*, 2024, **17**(2), e5173, DOI: **10.55905/revconv.17n.2-135**.